

Multiphasic growth dynamics of nanoparticle ensembles

Ji-Hyun Kim^{1,2,†}, Joodeok Kim^{3,4,†}, Byung Hyo Kim^{3,4,5,†}, Sanggeun Song^{1,2,6†}, Hoje Chun⁷,
Hyesung Choi^{3,4}, Jae Won Jung⁵, Youngju Sohn^{3,4}, Junhyeok Jeong^{3,4}, Kunwoo Park^{3,4},
Sungho Jeon⁸, Byungchan Han⁷, Won Chul Lee⁸, Jingyu Kang^{1,2,6}, Minho Lee^{1,2,6},
Taeghwan Hyeon^{3,4,*}, Jaeyoung Sung^{1,2,6,*}, Jungwon Park^{3,4,9,10,*}

¹ Creative Research Initiative Center for Chemical Dynamics in Living Cells, Chung-Ang University, Seoul 06974, Republic of Korea.

² Department of Chemistry, Chung-Ang University, Seoul 06974, Republic of Korea.

³ Center for Nanoparticle Research, Institute for Basic Science (IBS), Seoul 08826, Republic of Korea

⁴ School of Chemical and Biological Engineering, and Institute of Chemical Process, Seoul National University, Seoul 08826, Republic of Korea

⁵ Department of Organic Materials and Fiber Engineering, Soongsil University, Seoul 06978, Republic of Korea

⁶ National Institute of Innovative Functional Imaging, Chung-Ang University, Seoul 06974, Republic of Korea.

⁷ Department of Chemical and Biomolecular Engineering, Yonsei University, Seoul 03372, Republic of Korea.

⁸ Department of Mechanical Engineering, BK21 FOUR ERICA-ACE Center, Hanyang University, Ansan, Gyeonggi 15588, Republic of Korea.

⁹ Institute of Engineering Research, College of Engineering, Seoul National University, Seoul 08826, Republic of Korea

¹⁰ Advanced Institute of Convergence Technology, Seoul National University, Suwon-si, Gyeonggi-do 16229, Republic of Korea

[†] These authors contributed equally to this work.

*To whom correspondences should be addressed.

E-mail: thyeon@snu.ac.kr, jaeyoung@cau.ac.kr, or jungwonpark@snu.ac.kr

30 **Abstract**

31 Colloidal nanoparticles are of great interest in modern science and industry, yet the
32 thermodynamic origin of nanoparticle formation remains a mystery and nanoparticle growth
33 frequently exhibits nonclassical dynamics. Here, we tracked hundreds of *in-situ* growth
34 trajectories of a nanoparticle ensemble using an advanced liquid-phase-TEM, and discovered
35 that nanoparticle growth, including coalescence, exhibits monomer supply rate dependent
36 multiphasic dynamics, unexplainable by current theories. Motivated by this finding, we
37 developed a realistic model and statistical theories of growing nanoparticles, providing a
38 unified, quantitative understanding of the mean and fluctuation of nanoparticle size and size-
39 dependent growth rate across various nanoparticle systems and experimental conditions. Our
40 work reveals that the chemical potential in a nanoparticle has a finite maximum at a critical
41 size and exhibits a nonclassical dependence on nanoparticle size. This clear discrepancy from
42 the classical nucleation theory (CNT) results from the strongly non-extensive free energy
43 originating from nanoparticle motion, configurational degeneracy, and edge interaction, which
44 were neglected in the CNT. We also uncover how this chemical potential in a nanoparticle
45 governs formation and growth dynamics of an ensemble of nanoparticles, together with the
46 time-dependent monomer concentration in solution.

47

48 The properties of nanoparticles can be tuned by their size and shape, which makes them highly
49 attractive materials in both science and industry¹⁻³. For the last three decades, tremendous effort
50 has been devoted to synthesizing monodisperse nanoparticles of controlled sizes, shapes, and
51 compositions⁴⁻⁶, not only for investigating their unique physicochemical properties but also for
52 various applications such as quantum-dot-enhanced display⁷ and nanocatalysis⁸. Despite
53 extensive research, the thermodynamic origin of nanoparticle formation has not been
54 fundamentally understood and quantitative understanding of nanoparticle growth dynamics has
55 not been achieved⁹⁻¹¹.

56 Classical nucleation theory (CNT) based on the Gibbs-Thomson model cannot provide a
57 quantitative explanation of monodisperse nanoparticle formation^{12,13}. Early works by Frenkel¹⁴,
58 and Dillmann and Meier¹⁵ showed that the monodispersity of colloidal particles at a stationary
59 state under supersaturation cannot be accounted for by the usual equilibrium statistical
60 thermodynamics. Recently, a nonequilibrium nanoparticle growth process was recorded in real
61 time by liquid-phase transmission electron microscopy (TEM)¹⁶⁻¹⁸. Liquid-phase TEM of
62 individual nanoparticles revealed that the nanoparticle growth pathway is far more complex
63 than assumed in the classical crystallization model¹⁹⁻²². For example, TEM studies presented
64 direct evidence of nanoparticle coalescence and its contribution to the nanoparticle size
65 distribution²³. They also revealed that a specific surface selectively develops, while growth of
66 other surfaces is suppressed, to form faceted nanoparticles, in metal nanoparticles^{24,25}. Various
67 kinetic models have been proposed to explain the growth dynamics of nanoparticles^{9,12,13,26-28},
68 but none offer a quantitative or fundamental understanding. This is primarily due to the lack of
69 a realistic model of a nanoparticle and an accurate theory describing nanoparticle formation
70 and growth processes, in addition to the lack of large sets of experimental data showing the
71 detailed features of individual growth trajectories of nanoparticle ensembles¹⁶⁻¹⁸.

72 Here, we develop an advanced *in-situ* liquid-phase TEM and monitor an ensemble of
73 platinum nanoparticle growth trajectories. This direct observation reveals that nanoparticle
74 growth dynamics exhibits multiple kinetic phases. In each of the phases, the mean and variance
75 of nanoparticle size, the growth rate, and its size dependence exhibit their own distinct
76 dynamics, and all these features are sensitive to monomer supply rate. In addition,
77 nanoparticles undergo coalescence with a strongly time-dependent rate that transiently surges
78 and then vanishes. We find these experimental results unexplainable by current theories.
79 Motivated by these findings, we developed a realistic model of a nanoparticle and a statistical
80 mechanical theory. Our model and theory provide not only new physical understanding of
81 nanoparticle nucleation and growth dynamics but also a unified, quantitative explanation of the
82 time-dependent mean and fluctuation of nanoparticle size, and dynamics of the size-dependent
83 growth rate at all stages of nanoparticle growth for various nanoparticle systems under different
84 experimental conditions.

85 Our work reveals the chemical potential of a monomer in a nanoparticle has a finite
86 maximum value at a critical nanoparticle size and rapidly increases with the size for
87 nanoparticles with smaller than this critical size, in direct contradiction with the CNT. This
88 discrepancy from the CNT is caused by the strongly non-extensive free energy originating from
89 nanoparticle motion, configurational degeneracy, and edge interaction with the surrounding
90 environment, neglected in the CNT. This nonclassical size dependency of the chemical
91 potential plays an essential role in nanoparticle nucleation and multiphasic growth dynamics,
92 including transitions between slow and fast growth and between focusing and defocusing of
93 nanoparticle size.

94

95 ***In-situ* nanoparticle growth and classification of growth trajectories**

96 We observed an ensemble of growing metal nanoparticles in real-time using liquid-phase TEM
97 (Fig. 1a, Supplementary Videos 1-4). Multiple *in-situ* liquid-phase TEM movies were recorded,
98 which show growth processes of individual Pt and Au nanoparticles, under different reaction
99 conditions (Methods, Supplementary Video 1 for precursor Pt(acac)₂, Supplementary Video 3
100 for precursor Pt(COD)Cl₂, where Pt(acac)₂ has a platinum supplying rate higher than
101 Pt(COD)Cl₂ (Supplementary Fig. 1), and Supplementary Video 4 for precursor HAuCl₄). From
102 these movies, we tracked several hundred individual nanoparticle growth trajectories. To
103 accurately track size changes of hundreds of individual nanoparticles in the field of view of the
104 *in-situ* TEM movies, we developed an integrated image processing method, which includes
105 noise removal, edge-contrast optimization, and inconspicuous pixel removal to enhance edge
106 contrast while efficiently reducing noise from instruments and solvent background (Methods).
107 The processed TEM images were then converted via an adaptive binarization method where
108 the threshold for pixel assignment was determined by the locally averaged intensity of
109 neighboring pixels (Fig. 1b and Supplementary Fig. 2)²⁹. The resulting binarized image series
110 conserved the sizes and positions in the original liquid-phase TEM images and enabled
111 unbiased high-throughput measurement of the size and shape of all tracked nanoparticles
112 (Supplementary Videos 1-4, Supplementary Figs. 3-9). All growth trajectories that remained
113 in our field of view for 180 seconds in Supplementary Video 1, for 84 seconds in
114 Supplementary Video 3, and for 193.5 seconds in Supplementary Video 4 are collectively
115 presented in Fig. 1c.

116 We classified the growth trajectories of nanoparticles into two groups: one showing only
117 monomeric growth (Group-A) and the other exhibiting both monomeric growth and

118 coalescence growth (Group-B) (Fig. 1a). As these two groups exhibit qualitatively different
119 growth dynamics, we analyzed them separately²⁸. Group-A undergoing monomeric growth
120 makes the dominant contribution to the average size and the size distribution, and the size
121 distribution of Group-A is similar to the distribution of all nanoparticles including Group-A
122 and Group-B (Supplementary Fig. 10); for gold nanoparticles in Supplementary Video 4, there
123 is only Group-A in our experiment. To explain the growth dynamics of Group-A, we developed
124 a realistic model of a colloidal nanoparticle undergoing translation, rotation, and vibration, and
125 electronic interactions with the surrounding environment through its faces and edges. The
126 nanoparticle size-dependency of the Gibbs free energy of this nanoparticle model is
127 qualitatively different from the well-known Gibbs free energy profile assumed in the classical
128 nucleation theory and most current theories and its qualitative shape changes over time with
129 the monomer concentration or the chemical potential of monomers in solution (Fig. 1d).

130 **Monomeric growth dynamics**

131 Monomeric growth dynamics of nanoparticles is decomposable into multiple kinetic phases,
132 which are distinct for each monomer-precursor condition as shown in Fig. 1e (Phase-I-V for
133 platinum nanoparticles generated from precursor Pt(acac)₂, Phase-A-C for platinum
134 nanoparticles from Pt(COD)Cl₂, with a slower monomer supply rate than Pt(acac)₂, and Phase-
135 1-2 for gold nanoparticles generated from HAuCl₄). For platinum nanoparticle systems, the
136 mean and variance of the nanoparticle size exhibit rapid growth at the initial phase but slower
137 growth in the next phase and then the rapid growth again in the following phases. In comparison,
138 gold nanoparticles exhibit different growth dynamics (Supplementary Note 1 for the details of
139 the phase-dependent mean and variance in each nanoparticle system). We also measured the
140 size-dependent growth rate of nanoparticles at all times investigated, which is enabled by

141 tracking an ensemble of growth trajectories, and found that the size-dependency of the growth
142 rate also shows strongly dynamic phase-dependent behavior (Fig. 2).

143 To explain these experimental results, we developed a statistical mechanical theory for a
144 system of nanoparticles growing through reversible association with monomers in solution
145 (Methods). This theory provides a unified, quantitative explanation of various experimental
146 results including the time-profiles of the mean and variance of nanoparticle size, the size
147 distributions, and the size-dependent profiles of the growth rate at all times investigated (Figs.
148 1e and 2). We emphasize that our theory is based on a realistic nanoparticle model characterized
149 by six parameters that account for essential characteristics of a nanoparticle. Four of these
150 parameters characterize physical properties such as nanoparticle geometry, configurational
151 degeneracy, monomer energy in the face and on the edge of the nanoparticle, relative to the
152 monomer energy in the core. The remaining two parameters characterize the chemical
153 properties of the system, which are related to monomer solubility, the monomer diffusion
154 constant, and the bimolecular rate coefficient of monomer association. In Supplementary Table
155 1, we present the values of these parameters extracted from our analysis.

156 We considered a canonical ensemble of our model nanoparticle (Methods) and obtained
157 the monomer chemical potential in a single nanoparticle. As shown in Fig. 1d, the obtained
158 monomer chemical potential, μ_n^s , in an n -mer, a nanoparticle containing n monomers, has a
159 finite maximum at a critical size, in contrast with the Gibbs-Thomson equation underlying the
160 CNT, according to which the chemical potential diverges in the small size limit.

161 The analytic expression of μ_n^s is given by (Methods)

$$162 \quad \beta\mu_n^s - \beta\mu_\infty^s = \frac{c_1}{r/\sigma_s} + \frac{c_2}{(r/\sigma_s)^2} - \frac{4 + \alpha}{(r/\sigma_s)^3}. \quad (1)$$

163 Here, β and r denote, respectively, inverse thermal energy $(k_B T)^{-1}$, with k_B and T being the
 164 Boltzmann constant and absolute temperature, and the effective radius of a nanoparticle. r is
 165 related to the monomer number, n , in a nanoparticle by $n = (r/\sigma_s)^3 [\equiv 4\pi r^3 \rho_s / 3]$ with ρ_s
 166 being the monomer number density in the nanoparticle. c_1 and c_2 in the first two terms on
 167 the right-hand-side (r.h.s.) of equation (1) are given by $\frac{2}{3}c_f \Delta\varepsilon_f$ and $\frac{1}{3}c_e \Delta\varepsilon_e$, respectively,
 168 where c_f and c_e are nanoparticle-shape dependent parameters, and $\Delta\varepsilon_f$ ($\Delta\varepsilon_e$) denotes
 169 the free energy of a monomer at a facial (edge) site with respect to the free energy of a monomer
 170 at a bulk site in unit of thermal energy (Supplementary Note 2 for their precise definitions).
 171 $\Delta\varepsilon_f$ and $\Delta\varepsilon_e$ are dependent not only on microscopic properties of a nanoparticle but also on
 172 the environment surrounding the nanoparticle, including solvent and ligand molecules. $\Delta\varepsilon_f$
 173 or $\Delta\varepsilon_e$ is positive in general; however, $\Delta\varepsilon_e$ or c_2 can be negative because an atom or
 174 molecule can bind to a site with a lower coordination number stronger³⁰. α and α in the third
 175 term originate from the translational and rotational motion and the configurational degeneracy
 176 of a nanoparticle, respectively. The free energy associated with translational and rotational
 177 motion of a nanoparticle is proportional to $-4 \ln n$, which yields the chemical potential, $-4/n$,
 178 or $-4/(r/\sigma_s)^3$ in the third term (equation (10) in Methods). On the other hand, α is a constant
 179 that characterizes the n -dependence of the configurational degeneracy, Ω_n , of an n -mer, i.e.,
 180 $\Omega_n \propto n^\alpha$. For an n -mer with a small number, h , of vacant sites or defects, α is approximately
 181 the same as h , because the number of different defect configurations of the n -mer is given by
 182 $\Omega_n = n!/(n-h)!h! = n(n-1)\cdots(n-h+1)/h! \sim n^h$, when $h \ll n$. In units of thermal energy,
 183 the free energy associated with the configurational degeneracy is given by $-\ln \Omega_n = -\alpha \ln n$,

184 which yields the chemical potential, $-\alpha/n$, or $-\alpha/(r/\sigma_s)^3$ in the last term of equation (1).
 185 The second and third terms on the r.h.s. of equation (1) give the chemical potential, μ_n^s , its
 186 non-classical size dependency as demonstrated in Fig. 1d. For a large particle, the last two
 187 terms become negligible, and equation (1) reduces to the Gibbs-Thomson equation, where
 188 $\mu_n^s(r)$ monotonically decreases with size.

189 The non-classical size dependence of $\mu_n^s(r)$ plays a crucial role in the nucleation and
 190 growth dynamics. To explain, let us first consider a nanoparticle in a solution of monomers
 191 with a constant number density or chemical potential. If the chemical potential, μ_1 , of
 192 monomers in solution is higher than $\mu_n^s(r)$, the monomers in solution deposit onto the
 193 nanoparticle to increase the particle size. In the opposite case where $\mu_1 < \mu_n^s(r)$, the monomer
 194 in the nanoparticle dissolves into the solution to decrease the nanoparticle size. For this reason,
 195 the size approaches a particular size, r^* , at which $\mu_n^s(r^*) = \mu_1$ and $\partial\mu_n^s(r)/\partial r|_{r=r^*} > 0$ (Fig.
 196 1d). r^* is a stable fixed point because a nanoparticle with radius r smaller than r^* grows
 197 and a particle with r greater than r^* shrinks (Fig. 1d). This type of absolute size focusing is
 198 different from the size focusing observed for growing nanoparticles in Phase III, which is
 199 discussed below. Absolute size focusing occurs only when the largest nanoparticle in our
 200 system is smaller than the critical size, r^{**} , where $\mu_n^s(r^{**}) = \mu_1$ with $\partial\mu_n^s(r)/\partial r|_{r=r^{**}} < 0$.
 201 Note that r^{**} is an unstable fixed point around which a nanoparticle with $r < r^{**}$ shrinks
 202 and a nanoparticle with $r > r^{**}$ keeps growing, which is the classical Ostwald ripening. If
 203 $\mu_n^s(r)$ were a monotonically decreasing function of r , as described by the Gibbs-Thomson
 204 equation, absolute size focusing around the stable fixed point r^* would not have occurred;
 205 instead, only Ostwald ripening would have occurred.

206 The chemical dynamics of an ensemble of nanoparticles can be quantitatively understood
 207 by equation (1) and the well-known hierarchical kinetic equations for the concentration, ρ_n ,
 208 of n -mers, i.e., $\partial_t \rho_n(t) = J_{n-1}(t) - J_n(t)$, where the net growth rate J_n is given by
 209 $J_n = k_n^a \rho_1(t) \rho_n(t) - k_{n+1}^d \rho_{n+1}(t)$ ($n \geq 1$) and $J_0 = R_M - \sum_{m=1}^{\infty} J_m$ (Methods). Here, k_n^a and
 210 k_{n+1}^d denote the diffusion-influenced rate coefficients of monomer association with n -mers and
 211 dissociation from $(n+1)$ -mers, respectively. R_M denotes the rate of monomer supply defined
 212 by $R_M = \partial_t \rho_{1,T}$ with $\rho_{1,T}$ being the total monomer density, i.e., $\rho_{1,T}(t) = \sum_{n=1}^{\infty} n \rho_n(t)$. In our
 213 liquid TEM experiment, R_M is dependent on the intensity of electron irradiation and the
 214 reactivity of a precursor. It is difficult to measure R_M or $\rho_{1,T}(t)$ directly in our experiment;
 215 however, we circumvent this problem using the general relationship of $\rho_{1,T}(t)$ to the time-
 216 dependent mean nanoparticle size and the mean growth rate coefficient,
 217 $\langle j_n(t) \rangle = \langle J_n(t) / \rho_n(t) \rangle$ (Supplementary Notes 3 and 4 for the details).

218 In our model, k_n^a is not simply proportional to the surface area of the nanoparticle
 219 (Methods). Instead, the monomer association rate coefficient per nanoparticle area decreases
 220 with nanoparticle size. This is because the monomer association consists of two steps: the
 221 diffusion-limited encounter of monomers to an n -mer, whose rate coefficient, $k_D(n)$, is
 222 approximately given by $4\pi r D_1$ with r and D_1 being the nanoparticle radius and the diffusion
 223 coefficient of a monomer, and the ensuing association of monomers at the n -mer's surface,
 224 whose rate coefficient, $k_S(n)$, is proportional to the surface area, $4\pi r^2$, of nanoparticle, or
 225 $n^{2/3}$, i.e., $k_S(n) = 4\pi r^2 \kappa_a$ with κ_a being the proportionality constant. According to Collins-
 226 Kimball's theory³¹, k_n^a is given by $k_n^a \cong k_S(n) / [1 + k_S(n) / k_D(n)] = k_S(n) / [1 + (\kappa_a / D_1) r]$, so

227 that the association rate coefficient per nanoparticle surface area,
 228 $k_n^a/4\pi r^2 (= \kappa_a/[1 + (\kappa_a/D_1)r])$, decreases with the nanoparticle size (Supplementary Fig. 11).
 229 This form of k_n^a serves as a good approximation for a spherical nanoparticle when the
 230 reversibility of monomer association with a nanoparticle is not too large^{31,32}. In our analysis,
 231 we use a more elaborate form of k_n^a to account for a non-spherical geometry of nanoparticles,
 232 which may change over time during nanoparticle growth. The rate of monomer dissociation
 233 from a nanoparticle is not simply proportional to the surface area either, because it is connected
 234 to the monomer association rate by the detailed balance condition^{31,32} (Methods).

235 From the definition of growth rate J_n and the detailed balance condition, we derive the
 236 relationship between growth rate J_n and chemical potential μ_n^s given in equation (1) by

$$237 \quad J_n(t) = k_{n+1}^d \rho_{n+1} \left(e^{-\beta[\mu_n^s - \mu_1(t)]} \rho_n / \rho_{n+1} - 1 \right), \quad (n \geq 1) \quad (2)$$

238 where $\mu_1(t)$ denotes the chemical potential of monomers in solution, which logarithmically
 239 increases with monomer concentration, i.e., $\mu_1(t) = \mu_1^\circ + k_B T \ln \rho_1(t) / \rho^\circ$ with μ_1° and ρ°
 240 being the chemical potential and density of monomer in the standard-state solution,
 241 respectively [Methods for the derivation of equation (2)]. In equation (2) ρ_{n+1} / ρ_n can be
 242 replaced by unity whenever the nanoparticles have a continuous size distribution
 243 (Supplementary Fig. 12). Using our theory based on equations (1) and (2), we provide a unified,
 244 quantitative explanation of the time-dependent mean and fluctuation of the nanoparticle size
 245 and the size-dependent growth rate at all times for various nanoparticle systems under different
 246 experimental conditions (Methods and Figs. 1e and 2). From the quantitative analysis, we
 247 extracted the values of the five parameters characterizing the time-independent

248 physicochemical properties of nanoparticles for all experimental systems investigated
 249 (Supplementary Table 1). In addition, the time-dependent monomer concentration, or the
 250 monomer chemical potential in solution, and the shape index were extracted from the
 251 experimental data at each time frame (Fig. 4b,c).

252 In accordance with equation (2), the size-dependence of $J_n(t)$ always exhibits a far
 253 more dynamic phase-to-phase variation than the size distribution, $p_n(t) \left(\equiv \rho_n(t) / \sum_j \rho_j(t) \right)$,
 254 as shown in Fig. 2. This results from the time-dependent variation of monomer density or the
 255 chemical potential difference, $\mu_n^s - \mu_1(t)$, between a nanoparticle and solution in equation (2)
 256 (Fig. 3a,b). Since the first term in the parenthesis of equation (2) is the same as
 257 $k_n^a \rho_1 \rho_n / k_{n+1}^d \rho_{n+1}$ from the definition of J_n , $\mu_n^s - \mu_1(t)$ is practically the same as the free
 258 energy change per association of a monomer with an n -mer, $\exp[-\beta \Delta G_r(n \rightarrow n+1)]$
 259 $\left(= k_n^a \rho_1 \rho_n / k_{n+1}^d \rho_{n+1} \right)$ (Methods), whenever the nanoparticle size distribution is continuous, or
 260 whenever $\rho_n \cong \rho_{n+1}$. Therefore, if $\mu_n^s - \mu_1(t) [\cong \Delta G_r(n \rightarrow n+1)] < 0$, the association of
 261 monomers and n -mer occurs faster than the reverse dissociation reaction and the nanoparticle
 262 grow spontaneously; otherwise, the reverse dissociation reaction occurs faster than the
 263 association reaction and the nanoparticle shrink spontaneously.

264 Under the hyper-saturation condition, in which $\mu_n^s < \mu_1(t)$ for all n , nanoparticle growth
 265 occurs spontaneously for all sizes of nanoparticle and the growth rate coefficient
 266 $\mu_\infty^s < \mu_1(t) < \mu_n^s$, is positive for all n , which is the case in Phase-I, -III-V of platinum
 267 nanoparticles generated from precursor Pt(acac)₂, in Phase-A and-C of platinum
 268 nanoparticles from precursor Pt(COD)Cl₂, and in Phase-1 and-2 for gold nanoparticles from

269 precursor HAuCl_4 in our experiment (Fig. 3). The growth rate of nanoparticles increases with
270 μ_n^s . On the other hand, if μ_1 for some values of n , those n -mers with μ_n^s higher than μ_1
271 shrink and their growth rate coefficients j_n are negative, as shown in Phase II of platinum
272 nanoparticles generated from precursor $\text{Pt}(\text{acac})_2$. This transient decrease of nanoparticle size
273 can occur even under supersaturation condition, as shown in Phase B in Fig. 3.

274 By analyzing the “time-dependent” experimental data for the size-dependent growth rate
275 and size distribution for *in-situ* growth of metal nanoparticles under different precursor
276 conditions using equation (2), we can reconstruct the “time-independent” size dependence of
277 $\mu_n^s - \mu_\infty^s$ using the time-profiles of the solution-phase chemical potential $\mu_1(t)$ extracted
278 from our analysis (Fig. 4a,b). These reconstructed chemical potential differences are found to
279 be in good agreement with equation (1), which are independent of the monomer supply rate
280 either. Note that this chemical potential difference is exactly the same as $\ln(k_{n+1}^d/k_n^a \rho_{1,\infty})$ with
281 $\rho_{1,\infty}$ being the equilibrium solubility of monomers, because of the detailed balance condition
282 (Methods).

283 In order to demonstrate the general applicability of our model and theory, we also
284 analyzed experimental data for *ex-situ* growth of iron oxide and CdSe nanoparticles
285 synthesized using conventional heat-up⁵ and hot-injection methods³³, respectively (Methods).
286 We confirmed that our model and theory, without any modification, provide a quantitative
287 explanation of these *ex-situ* nanoparticle growth data (Supplementary Fig. 13).

288 According to our analysis, $\Delta\varepsilon_f (\propto c_1)$, or the free energy of a monomer at a facial site,
289 in equation (1) has positive values ; however, $\Delta\varepsilon_e (\propto c_2)$, or the free energy of a monomer at
290 an edge site, has negative values for all nanoparticle systems investigated. $\Delta\varepsilon_e (\propto c_2)$

291 exhibits greater system-to-system variation than $\Delta\varepsilon_f$ ($\propto c_1$) (Supplementary Table 1). Both
292 $\Delta\varepsilon_f$ and $\Delta\varepsilon_e$ increase the maximum value μ_n^{s*} of μ_n^s (Supplementary Fig. 14a,b).
293 However, compared with $\Delta\varepsilon_e$, $\Delta\varepsilon_f$ has a dominant effect on the μ_n^{s*} value. For example,
294 the value of n^* is found to be 1.06, 0.91, 0.79, and 0.74 in descending order for Iron oxide,
295 gold, CdSe, and platinum nanoparticles, respectively, for which μ_n^s values are also in a
296 descending order, given by 4.89, 4.33, 3.41, and 2.87 but μ_n^{s*} values are in an ascending order,
297 given by -5.06, -4.93, -2.82 and, -1.71, in unit of thermal energy. The critical nanoparticle size
298 $\Delta\varepsilon_f$ at which n^* assumes its maximum value decreases with $\Delta\varepsilon_f$ and $\Delta\varepsilon_e$. The value of
299 μ_n^{s*} depends on n^* more sensitively than $\Delta\varepsilon_f$ does (Supplementary Fig. 14b and the
300 caption of Fig. 4).

301 We note that the time profile of the supersaturation ratio, $\tilde{\rho}_1$, defined by the ratio of
302 the monomer concentration ρ_1 to monomer solubility $\rho_{1,\infty}$, extracted for iron oxide
303 nanoparticle system, is similar to the results reported in ref.³⁴. Our quantitative analysis also
304 reveals that all nanoparticles in the systems we investigated have a geometry similar to a
305 truncated octahedron for all growth phases without showing a systematic time-dependence (Fig.
306 4c and Supplementary Fig. 15). All tracked nanoparticles in the observation time windows of
307 our *in-situ* and *ex-situ* experiments consistently show quasi-spherical morphology
308 (Supplementary Videos 1-4).

309 There exists a general relationship between the mean and variance of nanoparticle size,
310 which holds for any growing particle system. This relationship quantitatively explains the time
311 dependence of the relative variance of particle size for various nanoparticle systems (Fig. 4d).
312 The chemical dynamics of any growing particle system can be described by a hierarchical

313 kinetic equation with a suitable choice of growth rate J_n . For an arbitrary J_n , we find that
 314 the variance, $\sigma_n^2(t)$, and mean, $\langle n(t) \rangle$, of nanoparticle size satisfy $\partial_t \sigma_n^2(t) = \partial_t \langle n(t) \rangle$
 315 $+2\langle \delta n(t) \delta j_n(t) \rangle$ with $\langle \delta n(t) \delta j_n(t) \rangle [\equiv \langle n(t) j_n(t) \rangle - \langle n(t) \rangle \langle j_n(t) \rangle]$ denoting the cross
 316 correlation between n and j_n . We note that this equation can also be derived from the
 317 Chemical Fluctuation Theorem in ref³⁵ (Methods). This relationship between the mean and
 318 variance shows that the mean growth rate, $\partial_t \langle n(t) \rangle$, and the cross correlation, $\langle \delta n(t) \delta j_n(t) \rangle$,
 319 play an essential role in determining the time dependence of the variance. From this equation,
 320 we obtained a simple, approximate expression of the relative variance as a second-order
 321 polynomial in $\langle n(t) \rangle^{-1}$ [equation (13) in Methods], which provides a quantitative explanation
 322 of the monomer supply rate-dependent relative variance under certain conditions
 323 (Supplementary Fig. 16).

324 Our experimental results for platinum nanoparticle systems generated from the two
 325 precursors with different monomer supply rates clearly show that the nanoparticle growth
 326 dynamics is dependent on the monomer supply rate as well as on intrinsic properties of the
 327 nanoparticle system. For example, the relative variance of platinum nanoparticle size tends to
 328 decrease with time for the fast monomer supply condition while it shows the opposite trend for
 329 the slow supply condition (Fig. 4d).

330 It is noteworthy that our theory consistently explains platinum nanoparticles synthesized
 331 under different monomer supply conditions without changing the time-independent
 332 microscopic parameters characterizing our nanoparticle model (Supplementary Table 1 for the
 333 optimized parameter values). This consistency and applicability to three other nanoparticle
 334 systems, gold, iron oxide, and CdSe, demonstrate the robustness of our nanoparticle model and

335 theory, which confirms the importance of time-dependent monomer concentration and the
336 nonclassical chemical potential in nanoparticle originating from nanoparticle motion, edge
337 interaction, and configurational degeneracy for a quantitative understanding of growth
338 dynamics of a nanoparticle system.

339 **Coalescence growth dynamics**

340 Nanoparticles also grow via mutual coalescence (Fig. 5a)^{18,23,24,36}. The size of the coalescing
341 nanoparticle group, Group-B, abruptly increases over a short period of time (Fig. 5b) in contrast
342 with Group-A that grows continuously. Our experimental data show that platinum nanoparticle
343 coalescence transiently occurs only near the end of Phase-III in our experiment with precursor
344 Pt(acac)₂ (Fig. 5c), where monomeric growth is slow and the nanoparticles manifest a small
345 size fluctuation around the mean, i.e., 1.5 nm ± 0.2 nm, because of size focusing throughout
346 Phase-III. Thus, coalescing nanoparticles have similar radii (Fig. 5a,d). Both the coalescence
347 rate coefficient and the coalescence time distribution are unimodal functions of time (Fig. 5c,e).
348 Individual trajectories of coalescing nanoparticles clearly show that the nanoparticles, which
349 undergo random thermal motion, coalesce when their separation becomes approximately 5.87
350 nm, close to twice the sum of the nanoparticle radius and the ligand length (Fig. 5f and
351 Supplementary Table 2). The transient coalescence dynamics between growing nanoparticles
352 cannot be explained by the classical chemical kinetics or previously reported theories of
353 diffusion-influenced reaction kinetics for particles with constant size and diffusion coefficient³⁷.
354 The classical Smoluchowski coagulation kinetics³⁸ can explain size distributions of silver
355 nanoparticles growing mainly by aggregation³⁹. However, this theory is inapplicable to Group-
356 B in which nanoparticles grow by both monomeric addition and coalescence (Supplementary
357 Fig. 17), for which the nanoparticle size and hence diffusion coefficient depend on time.

358 We found it essential to account for two facts in understanding the transient coalescence
359 dynamics. First, nanoparticles are initially separated by a distance far greater than their
360 encounter distance, and second, growing nanoparticles undergo anomalous thermal motion
361 because their diffusion coefficient, inversely proportional to the nanoparticle size, decreases
362 with time (Fig. 5g). In addition, to achieve a quantitative explanation of our experimental data,
363 we assume that the coalescence propensity of nanoparticles greater than a particular size rapidly
364 decreases with size (Fig. 5h). To obtain a mathematical description of this coalescence model,
365 we extended the reduced distribution function formalism, developed for the molecular
366 diffusion-influenced reactions^{32,40}, to encompass growing nanoparticle systems (Methods). The
367 resulting kinetic equation successfully explains the time-profiles of the coalescence rate
368 coefficient and the distribution of coalescence time. According to our analysis, the onset of
369 coalescence is delayed because it takes time for initially separated nanoparticle pairs to form
370 reactive encounter pairs via thermal motion and the encounter pair formation is a rare event.
371 The coalescence time distribution is dependent on the system properties including initial
372 nanoparticle density, reactivity, and monomeric growth dynamics of nanoparticles
373 (Supplementary Fig. 18). The coalescence rate vanishes at times longer than 126 seconds not
374 only because the larger nanoparticles have a smaller diffusion-influenced rate but also because
375 they have a vanishingly small coalescence propensity.

376 **Discussion**

377 The chemical potential in a nanoparticle has a finite maximum value at a critical nanoparticle
378 size, according to equation (1). This is in direct contradiction with Gibbs-Thomson equation,
379 according to which the chemical potential in a nanoparticle diverges in the small size limit. The
380 stark difference of equation (1) from the Gibbs-Thomson equation arises because of strongly

381 non-extensive free energy originating from nanoparticle motion, configurational degeneracy,
382 and edge interaction with the surrounding environment, overlooked in the CNT. The CNT
383 based on the Gibbs-Thomson equation does provide a useful, approximate result for the
384 crystallization rate⁴¹; however by considering the strongly non-extensive free energy terms,
385 one can explain the nucleation-rate data more accurately than the CNT^{15,42}. Equation (1)
386 reduces to the Gibbs-Thomson equation for an immobile and spherical nanoparticle free of any
387 defect. However, even for a spherical nanoparticle, as long as it moves or has defects, the
388 monomer chemical potential has a finite maximum, satisfying equation (1).

389 The nonclassical size dependence of the chemical potential, μ_n^s , of a monomer in
390 nanoparticle, given in equation (1), influences the nucleation and growth dynamics of
391 nanoparticles. Since the chemical potential of monomer in a nanoparticle has a finite maximum
392 value, μ_n^{s*} , it is possible to introduce a new concept: the hyper-saturation condition, in which
393 the monomer chemical potential, μ_1 , in solution is higher than μ_n^{s*} . Under the hyper-
394 saturation condition, nanoparticle growth is a spontaneous process for all sizes of nanoparticles,
395 which is the case in Phase-I, III-V on the left panel and Phase-A and -C on the right panel of
396 Fig. 3. On the other hand, under the supersaturation condition in which $\mu_\infty^s < \mu_1 < \mu_n^{s*}$, those
397 nanoparticles with monomer chemical potential μ_n^s higher than μ_1 in solution shrink. This
398 causes the mean nanoparticle size to grow slowly or even shrinks transiently, as shown in
399 Phase-II in the left panel and Phase-B in the right panel of Fig. 1e.

400 As demonstrated in this work, the present theory based on equation (1) enables a unified,
401 quantitative explanation of growth dynamics of a nanoparticle ensemble for various systems
402 under different experimental conditions, only when it is combined with equation (2), the new

403 relationship of the net growth rate of a nanoparticle to the difference between the monomer
404 chemical potentials in a nanoparticle and in solution. Our quantitative analysis makes it possible
405 to extract size- and shape-dependent physicochemical properties of a nanoparticle system from
406 the nanoparticle growth dynamics data obtained under a given experimental condition (see, for
407 example, Supplementary Table 1). By repeating this theoretical analysis of nanoparticle growth
408 dynamics for various *in-situ* or *ex-situ* experiments, we can achieve quantitative understanding
409 of how various microscopic properties of nanoparticle depend on experimental conditions. This
410 information is useful for optimizing the experimental condition for the synthesis of
411 nanoparticles with desired properties.

412 Our *in-situ* liquid TEM experiment, combined with unbiased tracking of nanoparticle
413 ensembles, provides important insights for designing controlled nanoparticle synthesis. For
414 example, the size distribution of Group-A undergoing monomeric growth is narrower than that
415 of Group-B accompanying coalescence (Supplementary Fig. 19). This finding suggests that a
416 synthetic approach that drives more particles to follow the monomeric growth pathway will
417 enhance the monodispersity of the synthesized nanoparticles.

418 Nanoparticle nucleation and growth dynamics require further research. Liao *et al.*
419 showed that, at short times, all low index facets of platinum nanoparticles exhibit similar
420 growth rates, but at long times beyond our current experimental observation time window, the
421 {100} facets stop growing while the other facets keep growing, resulting in the formation of
422 cube-shaped nanoparticles at long times²⁵. To explain these phenomena, it is necessary to
423 consider the facet dependence of the monomer association rate and the monomer chemical
424 potential in a nanoparticle. Recent studies showed that crystallization in calcium carbonate
425 solutions occurs through multistage pathways involving an intermediate condensed phase^{43,44},

426 and that the size of perovskite nanocrystals formed in cesium lead halide solution is controlled
427 by the halide ion concentration in the solution⁴⁵. We plan to extend the present model and
428 theory to encompass these systems, which we leave for future investigation.

429

430 **References**

- 431 1 Talapin, D. V., Lee, J.-S., Kovalenko, M. V. & Shevchenko, E. V. Prospects of colloidal
432 nanocrystals for electronic and optoelectronic applications. *Chem. Rev.* **110**, 389-458
433 (2010).
- 434 2 Kovalenko, M. V. *et al.* Prospects of nanoscience with nanocrystals. *ACS nano* **9**, 1012-
435 1057 (2015).
- 436 3 Boles, M. A., Ling, D., Hyeon, T. & Talapin, D. V. The surface science of nanocrystals.
437 *Nat. Mater.* **15**, 141-153 (2016).
- 438 4 Murray, C., Norris, D. J. & Bawendi, M. G. Synthesis and characterization of nearly
439 monodisperse CdE (E= sulfur, selenium, tellurium) semiconductor nanocrystallites. *J.*
440 *Am. Chem. Soc.* **115**, 8706-8715 (1993).
- 441 5 Park, J. *et al.* Ultra-large-scale syntheses of monodisperse nanocrystals. *Nat. Mater.* **3**,
442 891-895 (2004).
- 443 6 Tian, N., Zhou, Z.-Y., Sun, S.-G., Ding, Y. & Wang, Z. L. Synthesis of tetrahedral
444 platinum nanocrystals with high-index facets and high electro-oxidation activity.
445 *science* **316**, 732-735 (2007).
- 446 7 Shirasaki, Y., Supran, G. J., Bawendi, M. G. & Bulović, V. Emergence of colloidal
447 quantum-dot light-emitting technologies. *Nat. Photonics* **7**, 13 (2013).
- 448 8 Liu, L. & Corma, A. Metal catalysts for heterogeneous catalysis: from single atoms to
449 nanoclusters and nanoparticles. *Chem. Rev.* **118**, 4981-5079 (2018).
- 450 9 Thanh, N. T., Maclean, N. & Mahiddine, S. Mechanisms of nucleation and growth of
451 nanoparticles in solution. *Chem. Rev.* **114**, 7610-7630 (2014).
- 452 10 Lee, J., Yang, J., Kwon, S. G. & Hyeon, T. Nonclassical nucleation and growth of
453 inorganic nanoparticles. *Nat. Rev. Mater.* **1**, 1-16 (2016).
- 454 11 Ou, Z., Wang, Z., Luo, B., Luijten, E. & Chen, Q. Kinetic pathways of crystallization
455 at the nanoscale. *Nat. Mater.* **19**, 450-455 (2020).
- 456 12 LaMer, V. K. & Dinegar, R. H. Theory, production and mechanism of formation of
457 monodispersed hydrosols. *J. Am. Chem. Soc.* **72**, 4847-4854 (1950).
- 458 13 Peng, X., Wickham, J. & Alivisatos, A. Kinetics of II-VI and III-V colloidal
459 semiconductor nanocrystal growth: “focusing” of size distributions. *J. Am. Chem. Soc.*
460 **120**, 5343-5344 (1998).

- 461 14 Frenkel, J. A general theory of heterophase fluctuations and pretransition phenomena.
462 *J. Chem. Phys.* **7**, 538-547 (1939).
- 463 15 Dillmann, A. & Meier, G. A refined droplet approach to the problem of homogeneous
464 nucleation from the vapor phase. *J. Chem. Phys.* **94**, 3872-3884 (1991).
- 465 16 Williamson, M., Tromp, R., Vereecken, P., Hull, R. & Ross, F. Dynamic microscopy
466 of nanoscale cluster growth at the solid–liquid interface. *Nat. Mater.* **2**, 532-536 (2003).
- 467 17 Liao, H.-G., Cui, L., Whitlam, S. & Zheng, H. Real-time imaging of Pt3Fe nanorod
468 growth in solution. *Science* **336**, 1011-1014 (2012).
- 469 18 Yuk, J. M. *et al.* High-resolution EM of colloidal nanocrystal growth using graphene
470 liquid cells. *Science* **336**, 61-64 (2012).
- 471 19 De Yoreo, J. J. *et al.* Crystallization by particle attachment in synthetic, biogenic, and
472 geologic environments. *Science* **349**, aaa6760 (2015).
- 473 20 Loh, N. D. *et al.* Multistep nucleation of nanocrystals in aqueous solution. *Nat. Chem.*
474 **9**, 77-82 (2017).
- 475 21 Yang, J. *et al.* Formation of two-dimensional transition metal oxide nanosheets with
476 nanoparticles as intermediates. *Nat. Mater.* **18**, 970-976 (2019).
- 477 22 Zhu, G. *et al.* Self-similar mesocrystals form via interface-driven nucleation and
478 assembly. *Nature* **590**, 416-422 (2021).
- 479 23 Zheng, H. *et al.* Observation of single colloidal platinum nanocrystal growth
480 trajectories. *Science* **324**, 1309-1312 (2009).
- 481 24 Liao, H.-G. & Zheng, H. Liquid cell transmission electron microscopy study of
482 platinum iron nanocrystal growth and shape evolution. *J. Am. Chem. Soc.* **135**, 5038-
483 5043 (2013).
- 484 25 Liao, H.-G. *et al.* Facet development during platinum nanocube growth. *Science* **345**,
485 916-919 (2014).
- 486 26 Talapin, D. V., Rogach, A. L., Haase, M. & Weller, H. Evolution of an ensemble of
487 nanoparticles in a colloidal solution: theoretical study. *J. Phys. Chem. B* **105**, 12278-
488 12285 (2001).
- 489 27 Baumgartner, J. *et al.* Nucleation and growth of magnetite from solution. *Nat. Mater.*
490 **12**, 310-314 (2013).
- 491 28 Habraken, W. J. *et al.* Ion-association complexes unite classical and non-classical
492 theories for the biomimetic nucleation of calcium phosphate. *Nat. Commun.* **4**, 1-12

493 (2013).

494 29 Bradley, D. & Roth, G. Adaptive thresholding using the integral image. *J. Graph. Tools*
495 **12**, 13-21 (2007).

496 30 Aarons, J. *et al.* Predicting the oxygen-binding properties of platinum nanoparticle
497 ensembles by combining high-precision electron microscopy and density functional
498 theory. *Nano Lett.* **17**, 4003-4012 (2017).

499 31 Collins, F. C. & Kimball, G. E. Diffusion-controlled reaction rates. *J. Colloid Sci.* **4**,
500 425-437 (1949).

501 32 Sung, J. & Lee, S. Nonequilibrium distribution function formalism for diffusion-
502 influenced bimolecular reactions: Beyond the superposition approximation. *J. Chem.*
503 *Phys.* **111**, 796-803 (1999).

504 33 Chen, O. *et al.* Synthesis of metal–selenide nanocrystals using selenium dioxide as the
505 selenium precursor. *Angew. Chem. Int. Ed.* **120**, 8766-8769 (2008).

506 34 Kwon, S. G. *et al.* Kinetics of monodisperse iron oxide nanocrystal formation by
507 “heating-up” process. *J. Am. Chem. Soc.* **129**, 12571-12584 (2007).

508 35 Park, S. J. *et al.* The Chemical Fluctuation Theorem governing gene expression. *Nat.*
509 *Commun.* **9**, 1-12 (2018).

510 36 Wang, F., Richards, V. N., Shields, S. P. & Buhro, W. E. Kinetics and mechanisms of
511 aggregative nanocrystal growth. *Chem. Mater.* **26**, 5-21 (2014).

512 37 Rice, S. A. *Diffusion-limited reactions.* (Elsevier, 1985).

513 38 Smoluchowski, M. v. Drei vortrage uber diffusion, brownsche bewegung und
514 koagulation von kolloidteilchen. *Z. Phys.* **17**, 557-585 (1916).

515 39 Woehl, T. J. *et al.* Direct observation of aggregative nanoparticle growth: Kinetic
516 modeling of the size distribution and growth rate. *Nano Lett.* **14**, 373-378 (2014).

517 40 Lee, S. & Karplus, M. Kinetics of diffusion-influenced bimolecular reactions in
518 solution. I. General formalism and relaxation kinetics of fast reversible reactions. *J.*
519 *Chem. Phys.* **86**, 1883-1903 (1987).

520 41 Lupi, L. *et al.* Role of stacking disorder in ice nucleation. *Nature* **551**, 218-222 (2017).

521 42 Prestipino, S., Laio, A. & Tosatti, E. Systematic improvement of classical nucleation
522 theory. *Phys. Rev. Lett.* **108**, 225701 (2012).

523 43 Henzler, K. *et al.* Supersaturated calcium carbonate solutions are classical. *Sci. Adv.* **4**,
524 eaao6283 (2018).

525 44 Tribello, G. A., Bruneval, F., Liew, C. & Parrinello, M. A molecular dynamics study
526 of the early stages of calcium carbonate growth. *J. Phys. Chem. B* **113**, 11680-11687
527 (2009).

528 45 Dong, Y. *et al.* Precise control of quantum confinement in cesium lead halide perovskite
529 quantum dots via thermodynamic equilibrium. *Nano Lett.* **18**, 3716-3722 (2018).

530 46 Kim, B. H. *et al.* Critical differences in 3D atomic structure of individual ligand-
531 protected nanocrystals in solution. *Science* **368**, 60-67 (2020).

532 47 McClurg, R. B., Flagan, R. C. & Goddard III, W. A. Free energy and surface tension
533 of arbitrarily large Mackay icosahedral clusters. *J. Chem. Phys.* **102**, 3322-3330 (1995).

534 48 McClurg, R. B., Flagan, R. C. & Goddard III, W. A. Thermodynamic properties and
535 homogeneous nucleation rates for surface-melted physical clusters. *J. Chem. Phys.* **105**,
536 7648-7663 (1996).

537 49 Galimberti, D. R. & Sauer, J. Chemically Accurate Vibrational Free Energies of
538 Adsorption from Density Functional Theory Molecular Dynamics: Alkanes in Zeolites.
539 *J. Chem. Theory Comput.* **17**, 5849-5862 (2021).

540 50 Baletto, F. & Ferrando, R. Structural properties of nanoclusters: Energetic,
541 thermodynamic, and kinetic effects. *Rev. Mod. Phys.* **77**, 371 (2005).

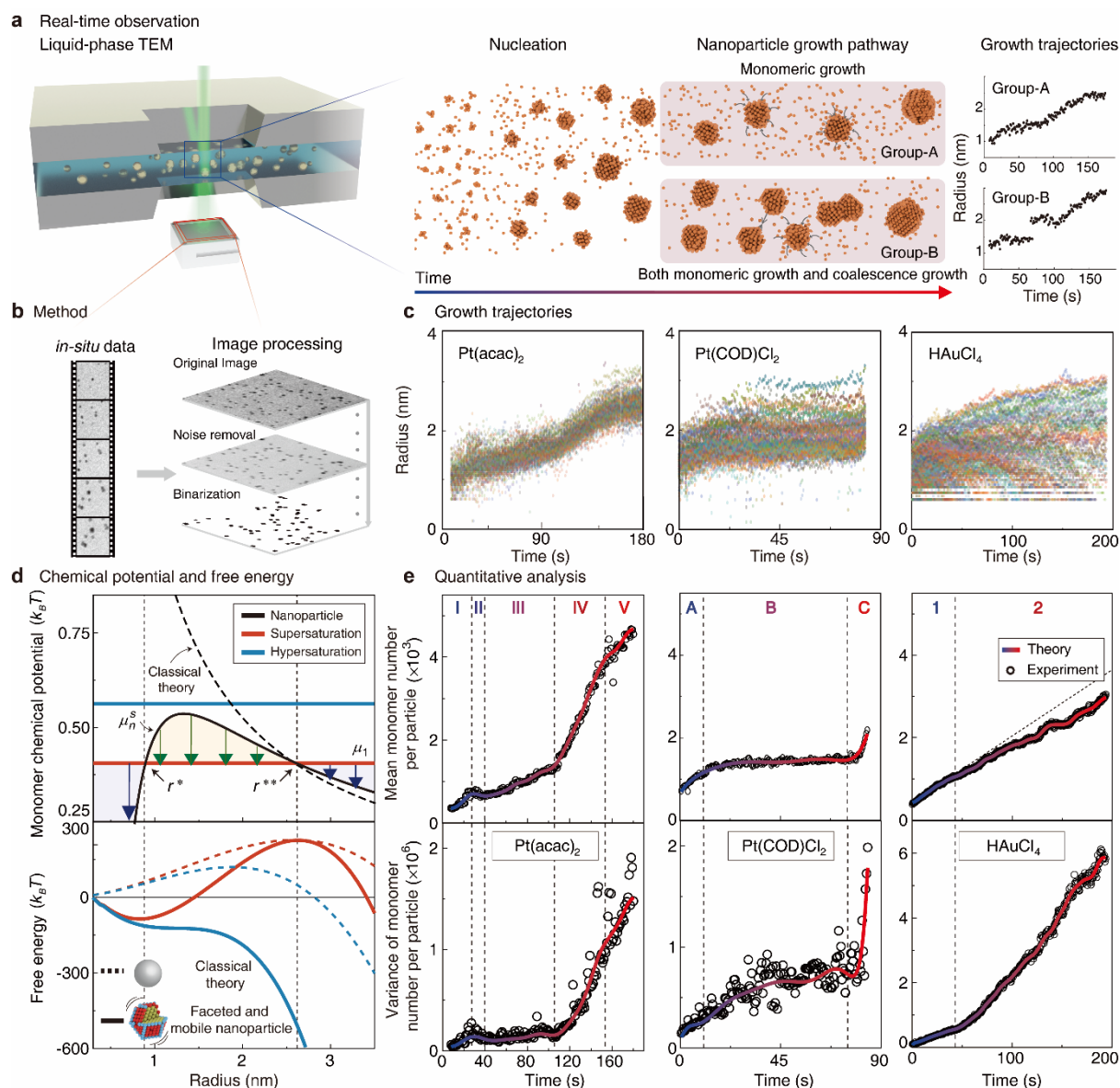
542 51 McQuarrie, D. A. & Simon, J. D. *Physical chemistry: a molecular approach*. Vol. 1
543 (University science books Sausalito, CA, 1997).

544 52 McQuarrie, D. A. *Statistical mechanics*. (Sterling Publishing Company, 2000).

545 53 Kang, J. S. J., Provost, S. B. & Ren, J. Moment-based density approximation techniques
546 as applied to heavy-tailed distributions. *Int. J. Stat. Prob.* **8**, 1-1 (2019).

547

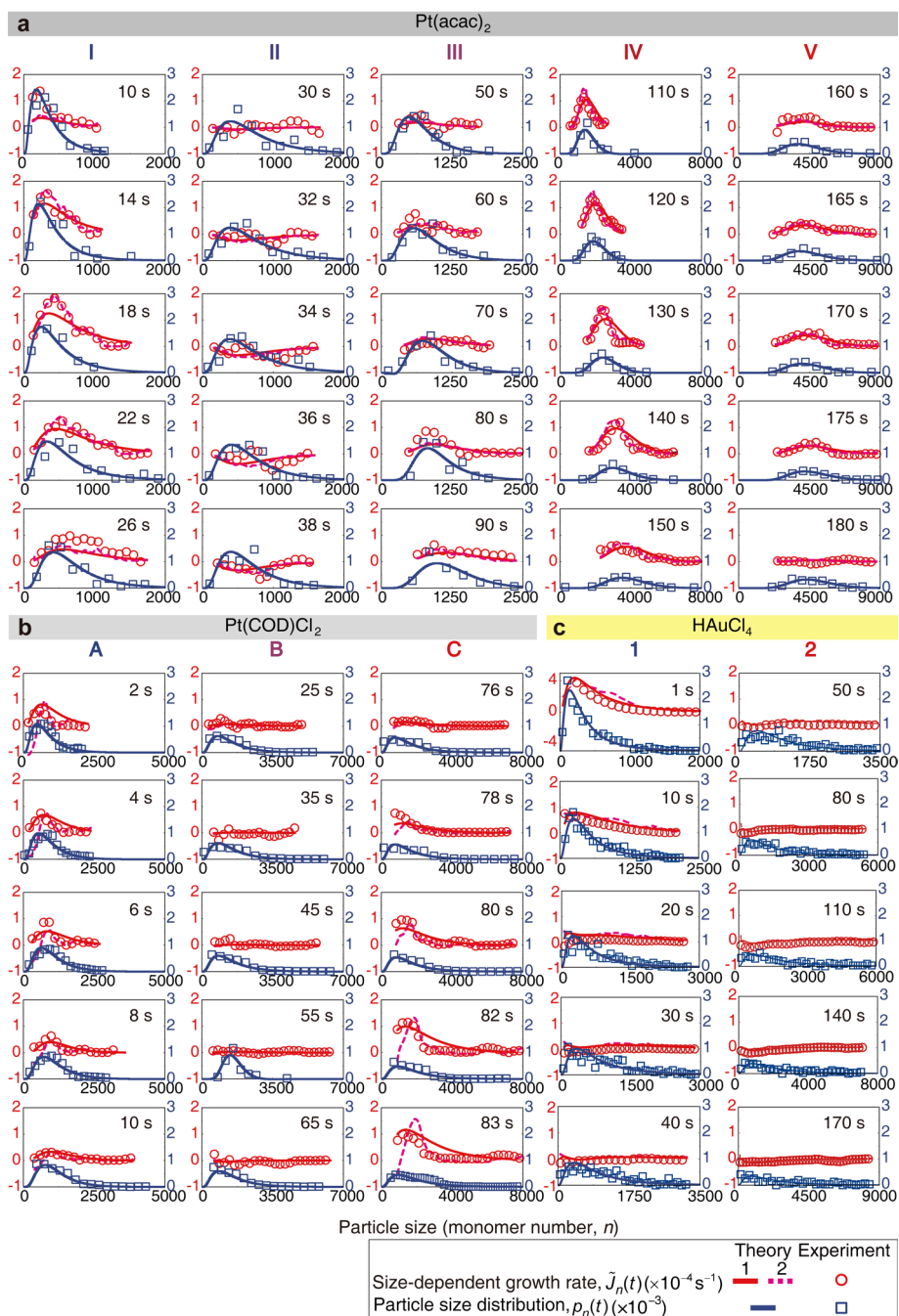
548



549

550 **Fig. 1. Thermodynamic origin of nanoparticle formation and multiphasic growth**
 551 **dynamics of nanoparticle ensembles.** **a**, Schematic of our experimental measurement of
 552 individual growth trajectories of metal nanoparticle ensemble. Left: real time *in-situ*
 553 observation of nanoparticle growth using a liquid-phase TEM. Center: Group-A showing only
 554 monomeric growth and Group-B exhibiting both monomeric growth and coalescence growth.
 555 Right: the pathway-dependent growth trajectories for platinum nanoparticles. **b**, Schematic of
 556 TEM image processing including noise removal, edge-contrast optimization, adaptive
 557 binarization, and inconspicuous pixel removal to convert *in-situ* TEM images into binarized
 558 images. **c**, Individual growth trajectories of hundreds of metal nanoparticles obtained using
 559 different precursors. Left: Pt(acac)₂. Center: Pt(COD)Cl₂. Right: HAuCl₄. **d**, Top: Chemical
 560 potential, μ_n^s , of monomers in a nanoparticle for our faceted and mobile nanoparticle model
 561 (black solid line) and for the classical immobile sphere model (black dashed line), and chemical
 562 potential, μ_1 , of monomers in supersaturated solution (red line) and in hypersaturated solution
 563 (blue line). For the hypersaturated solution, μ_1 is larger than the maximum of μ_n^s . Absolute

564 size-focusing occurs for nanoparticles with sizes close to r^* until reaching this value, while
565 nanoparticles with size close to r^{**} undergo Ostwald ripening (main text). Bottom: the
566 corresponding Gibbs free energy change associated with the formation of a nanoparticle from
567 monomers for our faceted and mobile nanoparticle model (solid line) and for the classical
568 immobile sphere model (dashed line): supersaturated solution (red) and hypersaturated solution
569 (blue). **e**, Comparison between theory and experiment for the mean and variance of the
570 monomer number per particle: experimental results (circles) and the theoretical results (lines).
571



572

573 **Fig. 2. Size-dependent growth rate and size distribution of nanoparticles at various times.**

574 Experimental data (symbols) and theoretical results (lines) (Methods) for scaled size-dependent

575 growth rate $\tilde{J}_n(t) [\equiv J_n(t)/\rho_{1,T}(t_0)]$ in unit of s^{-1} (red) and nanoparticle size distribution $p_n(t)$

576 (blue): $\tilde{J}_n(t)$ calculated from equation (2) or (S4-9) obtained using the theoretical size

577 distributions (solid line) or experimental size distributions (dashed line). Here, $\rho_{1,T}(t_0)$

578 denotes the value of the total monomer density, $\rho_{1,T}(t)$, at the beginning of our measurement

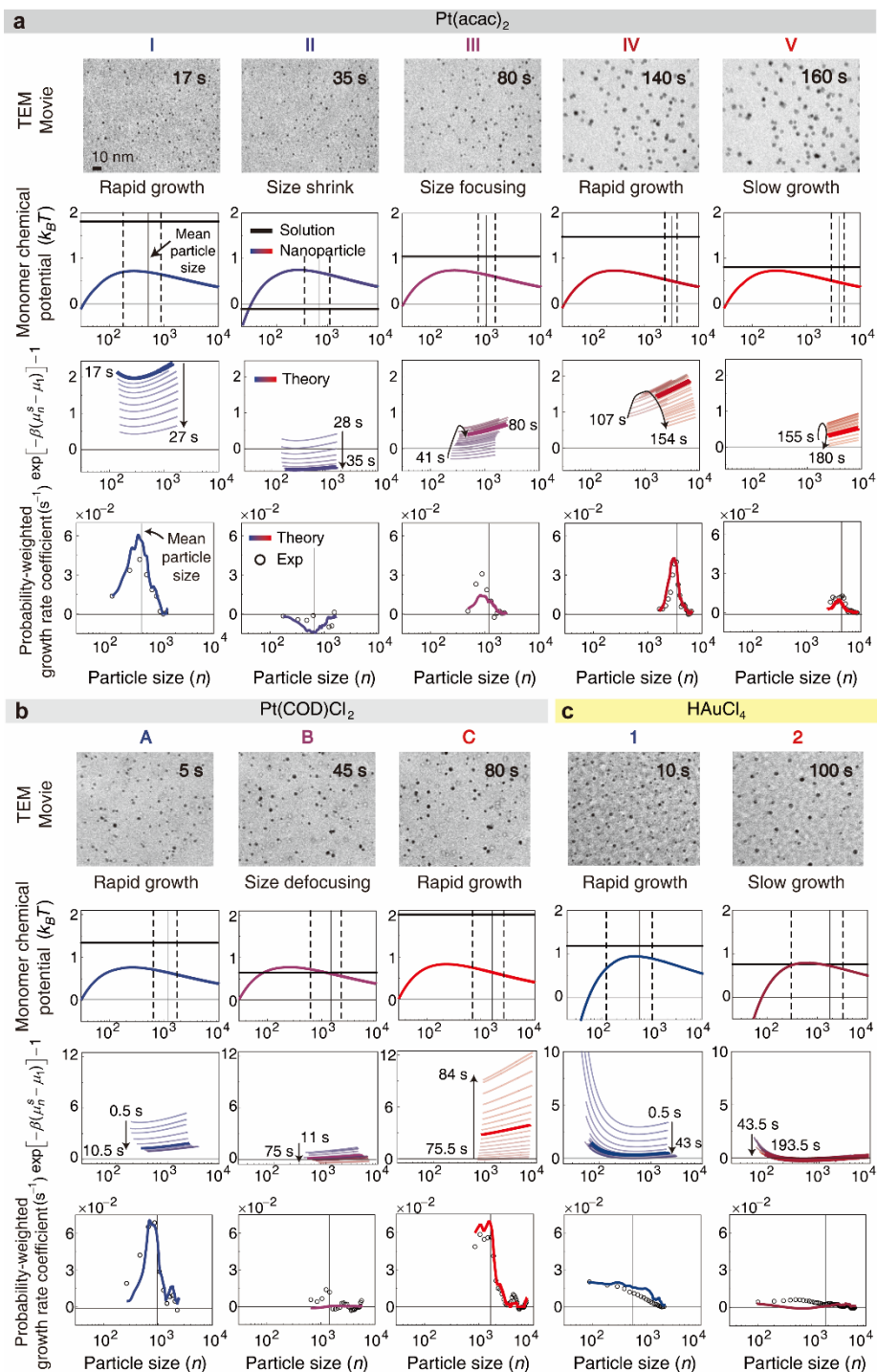
579 (see Supplementary Note 4 for the calculation method of $\tilde{J}_n(t)$). **a**, Results for Pt nanoparticles

580 generated from precursor Pt(acac)₂. In Phase-I, the growth rate is positive and a unimodal

581 function of size. However, in Phase-II, the growth rate can be a convex or concave function,

582 taking on small positive or even negative values. In Phase-III, the growth rate becomes positive
583 again but with far smaller magnitudes than Phase-I or -IV. In Phase-IV, the growth rate resumes
584 a unimodal size dependence but assumes its maximum at sizes far greater than in Phase-I. In
585 Phase-V, the growth rate decreases. **b**, Results for Pt nanoparticles from precursor Pt(COD)Cl₂,
586 which has a slower platinum supplying rate than Pt(acac)₂. In Phase-A, the growth rate is a
587 unimodal function of size, whose peak height decreases with time. In Phase-B, the growth rate
588 plateaus with little fluctuation around zero. In Phase-C, the growth rate resumes a unimodal
589 dependence on size, but the peak height tends to increase with time unlike Phase-A. **c**, Results
590 for Au nanoparticles generated from precursor HAuCl₄. In Phase-1, the growth rate exhibits a
591 similar trend as that for Phase-A in **b**. In Phase-2, the growth rate is slightly negative at small
592 sizes but has small positive values over a wide range of sizes, causing a positive slope of the
593 mean size for gold nanoparticles in Fig. 1e. Our theoretical results for $p_n(t)$ are in quantitative
594 agreement with experimental results at all times and under different monomer supply
595 conditions (Methods).

596

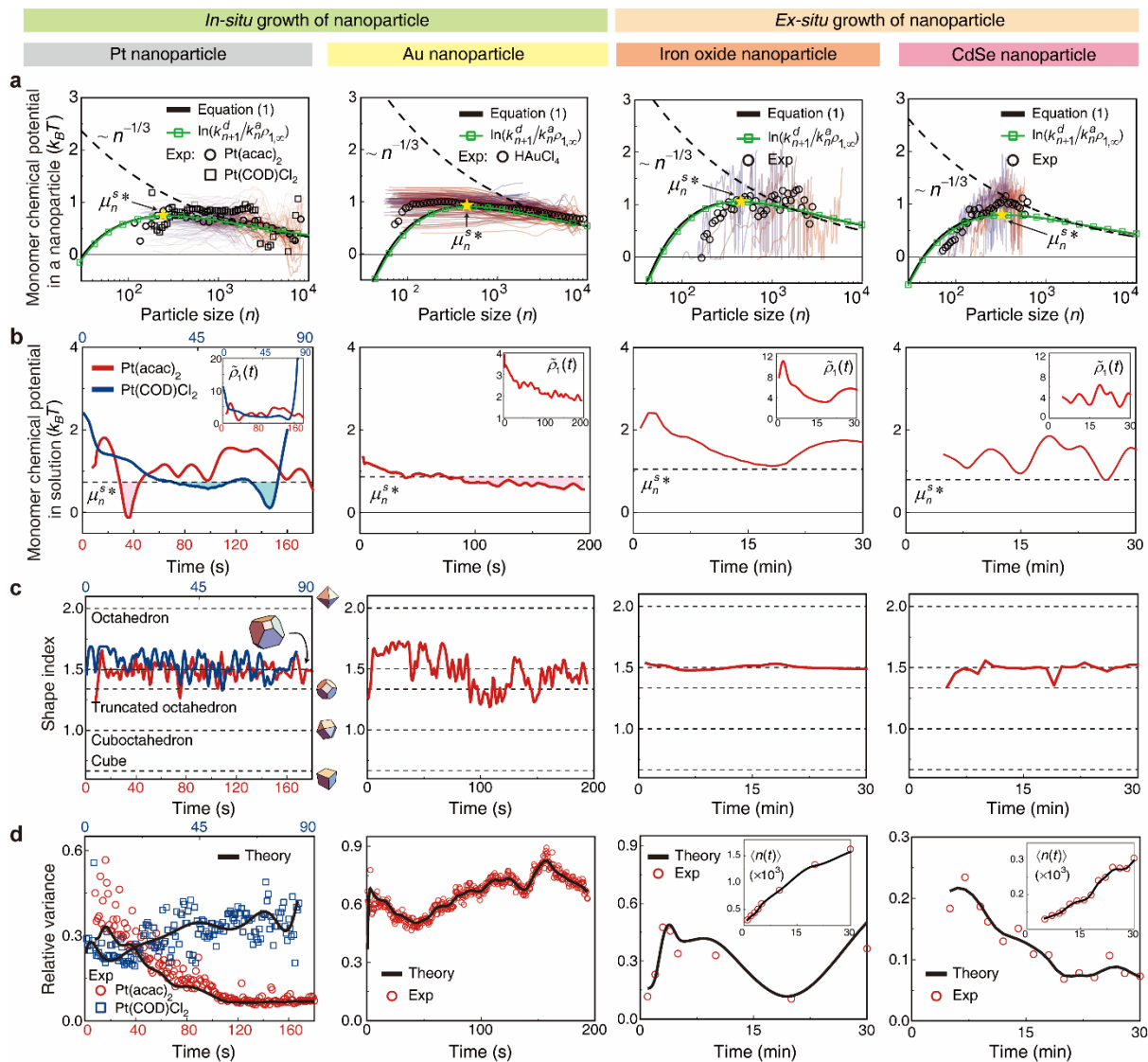


597

598 **Fig. 3. Phase-dependent dynamics of nanoparticle growth.** 1st row: TEM image. 2nd row:
 599 Monomer chemical potential, μ_n^s , in nanoparticle phase (colored solid line) and monomer
 600 chemical potential, μ_1 , in solution phase (black solid line): the mean particle size (vertical
 601 solid line) and error bar (vertical dashed lines). 3rd row: $\exp[-\beta(\mu_n^s - \mu_1(t))]-1$ with
 602 $\beta = 1/k_B T$. $\mu_n^s - \mu_1(t)$ is essentially the same as $\Delta G_r(n \rightarrow n+1) [= -k_B T$
 603 $\times \ln(k_n^a \rho_1 \rho_n / k_{n+1}^d \rho_{n+1})]$ (main text) and is exactly the same as $\Delta G_{n+1} - \Delta G_n (\cong \partial \Delta G_n / \partial n)$,

604 where ΔG_n denotes the free energy change associated with the formation of an n -mer from
605 n monomers, which has been frequently used in the CNT (see equation (10) in Methods for the
606 precise definition of ΔG_n and Supplementary Fig. 20 for the time-dependent change of ΔG_n
607 for various n). 4th row: Probability-weighted growth rate coefficient, $p_n j_n$: experimental data
608 (circles) and theoretical results (colored lines). p_n and j_n respectively denote the
609 nanoparticle size distribution and growth rate coefficient defined by $j_n \equiv J_n / \rho_n$ [see equation
610 (2) for J_n and ρ_n]. **a,b**, Results for Pt nanoparticles generated from precursor Pt(acac)₂ and
611 from precursor Pt(COD)Cl₂ with a slower monomer supplying rate than Pt(acac)₂. **c**, Results
612 for Au nanoparticles generated from precursor HAuCl₄.

613

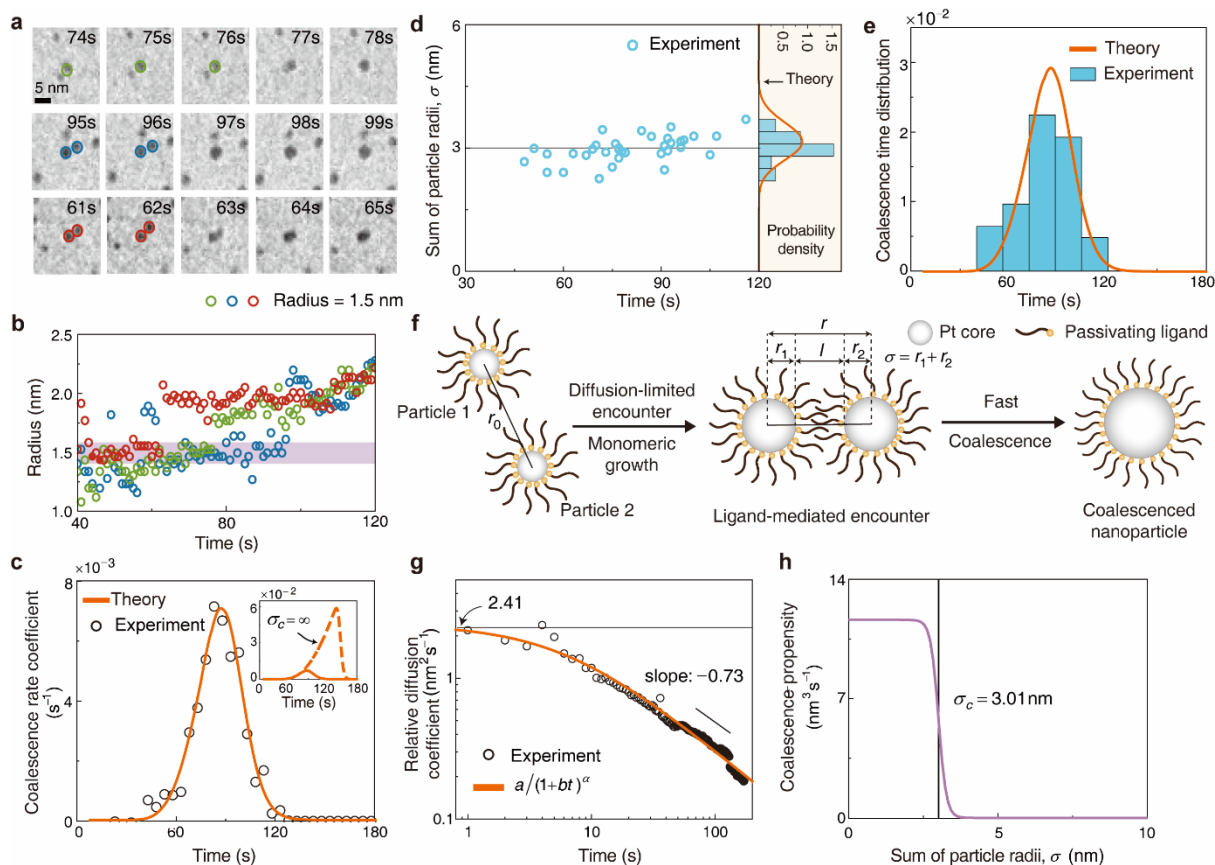


614

615 **Fig. 4. Physicochemical properties of our colloidal nanoparticle system.** Left: Results for
 616 *in-situ* growth of platinum nanoparticles (1st column) and gold nanoparticles (2nd column).
 617 Right: Results for *ex-situ* growth of iron oxide nanoparticles (3rd column) and CdSe
 618 nanoparticles (4th column). **a**, Chemical potential, μ_n^s , in a nanoparticle. The results extracted
 619 from the size-dependent growth rate data using equation (2): 1st column: Pt(acac)₂ (circles) and
 620 Pt(COD)Cl₂ (squares), and other nanoparticles (circles). The results for individual trajectories
 621 at short times (blue thin line) and at long times (red thin line). The result of equation (1) with
 622 the optimized parameter values in Supplementary Table 1 (black solid line), which is exactly
 623 the same as the logarithm of the ratio between k_{n+1}^d and $k_n^a \rho_{1,\infty}$ (green line with squares). The
 624 maximum value, μ_n^{s*} , of the chemical potential at $n = n^*$ is marked by the yellow star:
 625 $(n^*, \mu_n^{s*}/k_B T) = (272, 0.74)$, $(481, 0.91)$, $(446, 1.06)$, and $(359, 0.79)$ for platinum, gold
 626 iron oxide, and CdSe nanoparticle systems. The result of the Gibbs-Thomson equation (dashed line).
 627 k_n^a , k_{n+1}^d , and $\rho_{1,\infty}$ denote the rate coefficients of monomer association with n -mers and
 628 dissociation from $(n+1)$ -mers, and the equilibrium solubility of monomers, respectively. **b**,

629 Time profile of the chemical potential, μ_1 , in solution extracted from our analysis of the
 630 experimental data: 1st column: Pt(acac)₂ (red line) and Pt(COD)Cl₂ (blue line), and the other
 631 results (red line). Inset: corresponding supersaturation ratio, $\tilde{\rho}_1(t)$, related to μ_1 by
 632 $\mu_1(t) = \mu_\infty^s + k_B T \ln \tilde{\rho}_1(t)$ with μ_∞^s denoting the chemical potential in a macroscopic crystal
 633 (Methods). The time profiles of $\tilde{\rho}_1(t)$ for platinum and CdSe nanoparticles show a far more
 634 complicated time dependence than those for gold and iron oxide nanoparticles that resembles
 635 the LaMer diagram. In **b**, the time region where $\mu_1 \leq \mu_n^{s*}$ (dashed line) is filled with a color:
 636 1st column: platinum from Pt(acac)₂ (pink) and Pt(COD)Cl₂ (cyan), 2nd column: gold (pink).
 637 Our *ex-situ* synthesis of iron oxide and CdSe occurs under hypersaturation conditions with
 638 $\mu_1 > \mu_n^{s*}$. **c**, Time profile of the nanoparticle shape index extracted from our analysis of the
 639 experimental data: 1st column: platinum from Pt(acac)₂ (red line), platinum from Pt(COD)Cl₂
 640 (blue line), and other nanoparticles (red line). Our result indicates that nanoparticles assume a
 641 truncated octahedron with shape index about 1.5 throughout our experiment. **d**, Relative
 642 variance of nanoparticle size: experimental data: 1st column: platinum from Pt(acac)₂ (red
 643 circle), platinum from Pt(COD)Cl₂ (blue square), and other nanoparticles (red circle), and
 644 theoretical results (solid line). Inset: Mean sizes for iron oxide and CdSe nanoparticles:
 645 theoretical results (lines) and experimental data (circles).

646



647

648 **Fig. 5. Frequent coalescence events at a specific nanoparticle size.** **a**, TEM images showing
 649 three representative coalescence events. Circle: 1.5 nm. Scale bar: 5 nm. **b**, Time-dependent
 650 radii of the three nanoparticles shown in **a**. Coalescence occurs when the nanoparticle radius is
 651 about 1.5 nm regardless of coalescing times. **c**, Time-dependent coalescence rate coefficient:
 652 theoretical results (solid line) and experimental data (circles). Inset: Coalescence rate
 653 coefficient calculated for hypothetical nanoparticle model with a size-independent coalescence
 654 propensity (dashed line). **d**, Coalescence times and sum of nanoparticle radii, σ , at each
 655 coalescence event (Methods). Right: Probability density of σ : experimental data (bars) and
 656 theoretical prediction (solid line). **e**, Coalescence time distribution: theoretical results (solid
 657 line) and experimental data (bar). **f**, Schematic of the nanoparticle coalescence process. **g**,
 658 Relative diffusion coefficient between a pair of growing nanoparticles. **h**, Size-dependent
 659 coalescence propensity extracted from our analysis. The coalescence propensity becomes
 660 vanishingly small for nanoparticles with values of σ far greater than 3.0 nm.

661

662 **Methods**

663 **Liquid cell TEM measurement.**

664 For the *in-situ* TEM experiment, we prepared a liquid cell compatible with normal TEM
665 holders. The liquid cell consists of two 100- μm -thick cell bodies, two 25-nm-thick Si_3N_4
666 windows, and a 100-nm-thick spacer. A precursor solution was prepared by mixing 10 mg of
667 $\text{Pt}(\text{acac})_2$ and 0.1 mL of oleylamine into 0.9 mL of dichlorobenzene, and 0.4 μL of the solution
668 was loaded into the reservoir of the cell. After absorbing the excess solution with filter paper,
669 the liquid cell was sealed with a 600 μm aperture grid using vacuum grease. The growth of the
670 nanoparticles was monitored using JEOL 2010 at an acceleration voltage of 200 kV. The *in-*
671 *situ* TEM images were obtained at a frame rate of 1 frame per second (fps) with a dose rate of
672 $\sim 1,500 \text{ e/s}\cdot\text{\AA}^2$. In Supplementary Video 3 where $\text{Pt}(\text{COD})\text{Cl}_2$ was used as a precursor instead
673 of $\text{Pt}(\text{acac})_2$, the TEM images were recorded at a frame rate of 2 fps to capture initially rapid
674 increases in the nanoparticle. In Supplementary Video 4, a precursor solution was prepared
675 using 0.5 mM of HAICl_4 and 25 mM of cetyltrimethylammonium bromide (CTAB) ligand with
676 water solvent. The TEM images were recorded at a frame rate of 2 fps.

677 **Image processing.**

678 Image processing was executed using MATLAB code developed by our group to reduce any
679 noise in the TEM images and to generate binarized images for exact assignment of particle size.
680 Gaussian noise in raw TEM images can lead to arbitrary pixels with high contrast, which
681 hampers the generation of binarized images. Therefore, the first step involved applying
682 Gaussian and Wiener filters to remove Gaussian noise. Subsequently, the edge contrast of the
683 particles was enhanced using local Laplacian filtering. Laplacian filtering helps remove
684 insignificant contrast changes and highlight higher contrast changes to improve the accuracy

685 of particle identification. Finally, the images were binarized with adaptive binarization using
686 the Bradley method²⁹ to correct the background noise in the liquid-phase TEM images. After
687 the binarization procedure, insignificant objects with a size lower than 4 pixels were removed.

688 **Ensemble analysis.**

689 Tracking nanoparticles was performed by comparing correlation factors, F , calculated with the
690 position and size of nanoparticles in a series of TEM images. The correlation factor, F , is
691 defined as $F = (x_{n+1} - x_n)^2 + (y_{n+1} - y_n)^2 + (S_{n+1}^{1/2} - S_n^{1/2})^2$, where x_n , y_n , and S_n respectively
692 denote the x , y coordinates, and area of a nanoparticle at the n th frame. Nanoparticles with the
693 minimum correlation factors in consecutive frames were grouped in the same trajectory. Image
694 drift was corrected using mean displacement of all the tracked particles. The particles moving
695 in and out of the fixed field of view in the *in-situ* TEM movie due to the drift were excluded
696 for further analysis. A watershed algorithm was used to isolate adjacently located particles. The
697 area where the electron beam was strongly irradiated for alignment was excluded from the
698 ensemble analysis, because the area may have different chemical conditions including an
699 unusually high monomer concentration.

700 **Chemicals.**

701 90% oleic acid, 98% $\text{FeCl}_3 \cdot 6\text{H}_2\text{O}$, 99.8% anhydrous methanol, 99.9% selenium dioxide, and
702 1-octadecene were purchased from Aldrich. 99.999% cadmium nitrate tetrahydrate, and 99%
703 myristic acid were purchased from Alfa Aesar. Tetrabutylammonium hydroxide (1M
704 solution in methanol) was purchased from Acros. 95% sodium oleate were purchased from
705 TCI. 98% sodium hydroxide was purchased from Samchun. All chemicals were used without
706 further purifications.

707 **Ex situ growth study of iron oxide nanoparticles.**

708 Iron-oleate complexes were synthesized by the two-phase reaction of $\text{FeCl}_3 \cdot 6\text{H}_2\text{O}$ and
709 sodium oleate as previously reported⁵ A reaction solution was prepared by dissolving 3.6 g
710 (4 mmol) of the iron-oleate complexes and 1.13 g (4 mmol) of oleic acid in 20 g of 1-
711 octadecene. The solution was degassed at 110 °C, heated to 320 °C at a heating rate of 3.3
712 °C/min, and aged at 320 °C under an inert atmosphere. Sample aliquots were collected at 1,
713 2, 3, 4, 5, 10, 20, and 30 min during aging at 320 °C. For purification, 0.1 mL aliquot samples
714 were mixed with 1 mL acetone and 0.1 mL hexane followed and then centrifuged at 13,000
715 rpm for 5 min. The purification was conducted two times for each sample. We dispersed the
716 aliquot samples in 0.4 mL of hexane and took their TEM image using JEM-2100F (JEOL
717 Inst.) with the magnification of $\times 100,000$ (Supplementary Fig. 21).

718 **Ex situ growth study of cadmium selenide nanoparticles.**

719 Cadmium myristate precursors were synthesized using cadmium nitrate solution and sodium-
720 myristate solution according to the previous literature with some modifications³³. The reaction
721 solution was prepared by dissolving 0.2268 g (0.4 mmol) of cadmium myristae and 0.0444 g
722 (0.4 mmol) of selenium dioxide in 25.2 mL of 1-octadecene. The solution was heated to 220
723 °C at a heating rate of 10 °C/min and aged at 220 °C in air. Sample aliquots were collected at
724 5, 7, 9, 10, 12, 14, 16, 18, 20, 22, 24, 26, 28, and 30 min during aging at 220 °C. For purification,
725 0.2 mL aliquot samples were mixed with 0.6 mL acetone and then centrifuged at 4,000 rpm for
726 5 min. The purification was conducted one time for each sample. We dispersed the aliquot
727 samples in 1 mL of toluene, measured their absorption using Optizen POP Bio, and took their
728 TEM image using JEM-2010 (JEOL Inst.) with the magnification of $\times 100,000$ (Supplementary
729 Fig. 22).

730 **Estimation of the number of monomers in a nanoparticle.**

731 Quantitative analysis of the sizes of individual nanoparticles was performed by applying our
732 computational algorithm to the binarized images. The size information of the individual
733 particles was obtained by counting the number of pixels in the area that represents the
734 individual particles in the binarized images. The effective radius, r , of a nanoparticle at a given
735 time is calculated from the area of the pixels using the relationship, $r = (S/\pi)^{1/2}$, where S
736 denotes the two-dimensional area of the pixels occupied by the nanoparticle. The number, n ,
737 of monomers in the nanoparticle was then estimated as $n \cong (r/\sigma_s)^3 = 4\pi r^3 \rho_s / 3$, exact for a
738 spherical nanoparticle. The discrepancy between the approximate atom number estimated by
739 this formula and the true atom number is small (Supplementary Note 5). Here, the value of the
740 monomer number density, ρ_s , of a platinum nanoparticle is given by $\rho_s = 6.33 \times 10^{21} \text{ nm}^{-3}$
741 calculated using the mean lattice constant, 3.983 Å, of Pt measured for a few-nanometer-sized
742 Pt particles⁴⁶, which is a little larger than the lattice constant, 3.924 Å, of Pt in the bulk solid
743 phase by ca. 1.5%. The value of the radius, σ_s , corresponding to the effective volume,
744 $\rho_s^{-1} (= 4\pi\sigma_s^3/3)$, per monomer inside a nanoparticle is given by $\sigma_s = 0.156 \text{ nm}$. With the
745 empirical atomic radius, 0.139 nm of Pt, the packing fraction amounts to 0.71, close to the
746 packing fraction, 0.74, of a face-centered cubic lattice, which is the crystal structure of the bulk
747 Pt. For gold nanoparticles, we adopted the σ_s value, 0.159 nm, corresponding to the density
748 of a macroscopic Au crystal. For iron oxide and CdSe nanoparticles, where it is hard to identify
749 a definite chemical composition of a single monomer, the values of σ_s were determined by
750 repeating the optimization procedure of our model to the experimental data for *ex-situ* growth
751 of the two nanoparticles with various values of σ_s , and choosing the best-fitted result: $\sigma_s =$
752 0.350 nm for iron oxide nanoparticles and $\sigma_s = 0.251 \text{ nm}$ for CdSe nanoparticles.

753 **Derivation of equation (1): the chemical potential of a monomer in a nanoparticle**
 754 **composed of n monomers.**

755 The chemical potential, μ_n^s , of a monomer in a nanoparticle containing n monomers, or an n -
 756 mer is related to the Helmholtz free energy, $F_n^s (= -k_B T \ln q_n)$, of a single n -mer as
 757 $\mu_n^s = F_{n+1}^s - F_n^s = -k_B T \ln(q_{n+1}/q_n)$. Here, q_n denotes the canonical partition function of a
 758 single n -mer in solution. q_n differs from the partition function of a single n -mer in gas phase
 759 due to interactions of the nanoparticle with the surrounding environment (Supplementary Note
 760 6); however, q_n can still be decomposed into the translational (q_{trans}), rotational (q_{rot}),
 761 vibrational (q_{vib}), electronic (q_{elec}) partition functions, i.e., $q_n = \Omega_n q_{trans}(n) q_{rot}(n) q_{vib}(n)$
 762 $\times q_{elec}(n)$ with Ω_n denoting the configurational degeneracy of an n -mer^{47,48}. Each partition
 763 function can be written as a function of n : $q_{trans} \propto n^{3/2}$, $q_{rot} \propto n^{5/2}$, $q_{vib} \propto e^{-\lambda n}$,
 764 $q_{elec} \propto q_b^{n_b} q_f^{n_f} q_e^{n_e}$, and $\Omega_n \propto n^\alpha$, leading to

$$765 \quad q_n = C e^{-\lambda n} n^{4+\alpha} q_b^{n_b} q_f^{n_f} q_e^{n_e} \quad (n \gg 1) \quad (3)$$

766 with C being the n -independent constant. In equation (3), λ is related to the normalized density,
 767 $\tilde{g}(\omega)$, of vibrational states by $\lambda = 3 \int_0^\infty d\omega \tilde{g}(\omega) [\beta \hbar \omega / 2 + \ln(1 - e^{-\beta \hbar \omega})]$ with \hbar being the
 768 Planck constant, h , divided by 2π . $\tilde{g}(\omega)$ is normalized such that the whole integration of
 769 $\tilde{g}(\omega)$ over vibrational frequency, ω , is equal to unity. We note that an anharmonic
 770 contribution to the vibrational partition function can also be accounted for using a suitable
 771 density of vibrational states⁴⁹. In equation (3), q_b and $q_f(q_e)$ stand for the electronic
 772 partition function of a monomer at a bulk site and a facial (edge) site of an n -mer, respectively.

773 $q_{f(e)}$ is dependent on the microscopic interaction of the nanoparticle face (edge) and the
 774 surrounding environment including ligand and solvent molecules. $n_{b(f \text{ or } e)}$ is the number of
 775 monomers located at bulk (facial or edge) sites, which depends on the size, $n(=n_b+n_f+n_e)$,
 776 and the geometry of a given nanoparticle.

777 We assume that the geometric shape of a nanoparticle is a non-regular truncated
 778 octahedron⁵⁰, whose geometric shape is completely determined by shape index δ . A truncated
 779 octahedron reduces to a regular cuboctahedron when $\delta=1$, a regular truncated octahedron
 780 when $\delta=4/3$, and a regular octahedron in the when $\delta=2$ (Supplementary Fig. 23). We
 781 derive the exact relationship of n_f and n_e to nanoparticle size n and shape index δ
 782 (Supplementary Note 7):

$$783 \quad n_f = \left[8 - 6\delta m - (3\delta^2 - 12\delta + 8)m^2 + \frac{3}{2}(2 - 2/m - \delta)^2 m^2 \Theta(2 - 2/m - \delta) \right] \Theta(m - 2), \quad (4a)$$

$$784 \quad n_e = 12(m - 1)\Theta(m - 1), \quad (1 \leq \delta < 2) \quad (4b)$$

785 where $\Theta(x)$ denotes Heaviside step function defined by $\Theta(x \geq 0) = 1$ and $\Theta(x < 0) = 0$.
 786 See equation (S7-6) for the expression of n_e when $\delta = 2$. From now on, we assume the value
 787 of δ is between 1 and 2. In equation (4), m is the real root of the following cubic equation:

$$788 \quad n = 1 + a_1 m + a_2 m^2 + a_3 m^3, \quad (5)$$

789 where $a_{i \in \{1,2,3\}}$ is a positive-valued function only of δ ($1 \leq \delta \leq 2$), explicitly, $a_1 = \frac{1}{2}\delta + \frac{4}{3}$,
 790 $a_2 = 2 - \frac{3}{4}(2 - \delta)^2$, and $a_3 = \frac{1}{4}(3 + (3 - \delta)^2)\delta - \frac{4}{3}$.

791 When the value of n is large, a simple approximate expression of m can be obtained from
 792 equation (5), which is given by $m \cong (n/a_3)^{1/3} - a_2/3a_3$. When n is greater than 170, the relative

793 error of this approximate expression for m is less than 1% regardless of the value of δ .
 794 Substituting this expression of m into equations (4a) and (4b) and taking the leading terms, we
 795 obtain the following analytic expressions of n_f and n_e : $n_f \cong [4 - 3(2 - \delta)^2](n/a_3)^{2/3}$ and
 796 $n_e \cong 12(n/a_3)^{1/3}$.

797 Using equation (3), we obtain the expression of the chemical potential,
 798 $\mu_n^s [= -k_B T \ln(q_{n+1}/q_n)]$, of a monomer in an n -mer as

$$799 \quad \beta\mu_n^s = -\ln(e^{-\lambda} q_b) - \Delta n_f \ln \frac{q_f}{q_b} - \Delta n_e \ln \frac{q_e}{q_b} - (4 + \alpha) \ln(1 + \frac{1}{n}), \quad (6)$$

800 where $\Delta n_{f,e}$ denotes the difference between $n_{f,e}$ of an $(n+1)$ -mer and $n_{f,e}$ of an n -mer,
 801 i.e., $\Delta n_{f,e} = n_{f,e}(n+1) - n_{f,e}(n)$. Δn_f and Δn_e decreases with n and vanish in the large n
 802 limit. On the r.h.s. of equation (6), the first term is the chemical potential, $\beta\mu_\infty^s$, of monomers
 803 in a macroscopic crystal. Equation (6) is essentially the same as equation (1) with $n = (r/\sigma_s)^3$,
 804 $\Delta\varepsilon_f = -\ln \frac{q_f}{q_b}$ and $\Delta\varepsilon_e = -\ln \frac{q_e}{q_b}$ (Supplementary Note 2 for more details). For immobile,
 805 perfect spheres free of configurational degeneracy, $\beta\mu_n^s - \beta\mu_\infty^s$ reduces to the Gibbs-
 806 Thomson equation, given by $\beta\mu_n^s - \beta\mu_\infty^s = c_1 \sigma_s / r$, shown as the dashed line in the upper panel
 807 of Fig. 1d (Supplementary Note 2). However, as long as it moves or has defects, the chemical
 808 potential of a monomer deviates from the Gibbs-Thomson equation and has a finite maximum,
 809 μ_n^{s*} , at a critical size due to the contribution from the last term on the r.h.s. of equation (1) or
 810 (6); for the spherical nanoparticle as well, the absolute size focusing is possible under
 811 supersaturation when the monomer chemical potential, μ_l , in solution is lower than μ_n^{s*} .

812 Free energy change

813 The free energy change, $\Delta G_r(n \rightarrow n+1)$, per association of a monomer with an n -mers
 814 is given by⁵¹

$$815 \quad \Delta G_r(n \rightarrow n+1) = \Delta G_r^\circ(n \rightarrow n+1) + k_B T \ln \frac{\rho_{n+1}/\rho^\circ}{(\rho_n/\rho^\circ)(\rho_1/\rho^\circ)} \quad (7)$$

816 with ρ° denote the density unit. At chemical equilibrium, we have $\Delta G_r(n \rightarrow n+1) = 0$ and

$$817 \quad \Delta G_r^\circ(n \rightarrow n+1) = -k_B T \ln K_{eq}(n \rightarrow n+1) \quad (8)$$

818 with $K_{eq}(n \rightarrow n+1)$ being the equilibrium constant, given by

$$819 \quad K_{eq}(n \rightarrow n+1) = (\rho_{n+1}^{eq}/\rho^\circ) / (\rho_n^{eq}/\rho^\circ)(\rho_1^{eq}/\rho^\circ) = \rho^\circ q_{n+1}^* / q_n^* q_1^* \quad \text{where } q_j^* \text{ denotes } q_j$$

820 divided by system volume⁵². Because of the detailed balance condition, i.e.,

$$821 \quad k_n^a \rho_1^{eq} \rho_n^{eq} = k_{n+1}^d \rho_{n+1}^{eq}, \quad K_{eq}(n \rightarrow n+1) \text{ is the same as } k_n^a \rho^\circ / k_{n+1}^d. \text{ Using this result, equations (7)}$$

822 and (8), we obtain

$$823 \quad \exp[-\beta \Delta G_r(n \rightarrow n+1)] = k_n^a \rho_1 \rho_n / k_{n+1}^d \rho_{n+1} \quad (9)$$

824 in the main text. Whenever the nanoparticle size distribution is continuous, $\Delta G_r(n \rightarrow n+1)$ is

825 essentially the same as $\mu_n^s - \mu_1$ as discussed in the main text. μ_1 denotes the chemical

826 potential of monomers in solution, given by $\mu_1 = -k_B T \ln(q_1^*/\rho_1)$ with ρ_1 and q_1^* being the

827 number density and the volume-scaled partition function of a monomer in the solution phase,

828 respectively.

829 $\Delta G_r(n \rightarrow n+1)$ or $\mu_n^s - \mu_1$ is the same as $\Delta G_{n+1} - \Delta G_n$ where ΔG_n denote the free

830 energy change, associated with the formation of an n -mer from n monomers in solution phase,

831 often discussed in the CNT. ΔG_n is given by $\Delta G_n = F_n^s - n\mu_1$ ¹⁵, where μ_1 . Substituting

832 equation (3) into this definition, we obtain

$$833 \quad \beta\Delta G_n = -\ln C - n_f \ln \frac{q_f}{q_b} - n_e \ln \frac{q_e}{q_b} - (4 + \alpha) \ln n - n \ln \frac{\rho_1}{\rho_{1,\infty}}, \quad (10)$$

834 where $\rho_{1,\infty}$ denotes the monomer solubility, or the concentration of monomers in the solution

835 phase that are in equilibrium with the macroscopic crystal. On the r.h.s. of equation (10),

836 $-4 \ln n$ and $-\alpha \ln n$ in the fourth term respectively originate from $-\ln[q_{trans}(n)q_{rot}(n)]$ and

837 $-\ln\Omega_n$, noting that $q_{trans} \propto n^{3/2}$, $q_{rot} \propto n^{5/2}$, and $\Omega_n \propto n^\alpha$; the differentiation of the free

838 energy term, $-(4 + \alpha) \ln n$, with respect to n yields $-(4 + \alpha)/n$, which is equivalent to the

839 last term on the r.h.s. of equation (1) when n is large enough such that $\ln(1 + n^{-1}) \cong n^{-1}$. $\rho_{1,\infty}$

840 is determined by equating the monomer chemical potentials, $\beta\mu_1 [= -\ln(q_1^*/\rho_1)]$ and

841 $\beta\mu_{n \rightarrow \infty}^s [= -\ln(e^{-\lambda} q_b)]$, yielding $\rho_{1,\infty} = e^\lambda q_1^*/q_b$. The monomer concentration, ρ_1 , scaled by

842 $\rho_{1,\infty}$ corresponds to the degree of supersaturation, $\tilde{\rho}_1$, i.e., $\tilde{\rho}_1 = \rho_1/\rho_{1,\infty}$. Equation (10)

843 reduces to the corresponding equations in refs^{15,42} when the numbers, n_f and n_e , of facial

844 and edge monomers are directly proportional to $n^{2/3}$ and $n^{1/3}$, respectively. In Fig. 1d, we

845 show the dependence of $\beta\mu_n^s - \beta\mu_\infty^s$ and $\beta\Delta G_n + \ln C$ on the nanoparticle radius, r , using

846 equations (6) and (10) with $n = (r/\sigma_s)^3$. For immobile, perfect spheres free of configurational

847 degeneracy, $\beta\Delta G_n + \ln C$ is given by $\beta\mu_n^s - \beta\mu_\infty^s = c_1 \sigma_s / r \beta\Delta G_n + \ln C$, shown in Fig. 1d

848 (see Supplementary Note 2 for the details).

849 **Derivation of equations (2): nanoparticle ensemble growth dynamics through monomer**
 850 **association.**

851 The nonequilibrium chemical dynamics of an ensemble of growing particles can be explained

852 by the well-known hierarchical kinetic equations:

$$853 \quad \partial_t \rho_n(t) = J_{n-1}(t) - J_n(t) \quad (n \geq 1) \quad (11)$$

854 with J_n being the growth rate of n -mers. $J_0(t)$ is related to all of the other $J_{n(\geq 1)}$'s by

$$855 \quad J_0 = \partial_t \rho_{1,T}(t) - \sum_{n=1}^{\infty} J_n, \text{ where } \rho_{1,T} \text{ denotes the total monomer density defined by}$$

$$856 \quad \rho_{1,T}(t) = \sum_{n=1}^{\infty} n \rho_n(t) \text{ with } \rho_n(t) \text{ denoting the number density of } n\text{-mers. Note that}$$

$$857 \quad J_n(t) = \partial_t \psi_{n+1}^d(t) \text{ is directly related to the time derivative of the cumulative density, } \psi_n^d(t)$$

$$858 \quad \left[\equiv \sum_{k=n}^{\infty} \rho_k(t) \right] \text{ by } J_n(t) = \partial_t \psi_{n+1}^d(t). \text{ When the total density of the nanoparticles,}$$

$$859 \quad \rho_c \left[\equiv \sum_{i=1}^{\infty} \rho_i \right] \text{ slowly varies over time, the following equations can be obtained from equation}$$

860 (11) (Supplementary Note 3):

$$861 \quad \partial_t \langle n(t) \rangle = \langle j_n(t) \rangle, \quad (12a)$$

$$862 \quad \partial_t \sigma_n^2(t) = \partial_t \langle n(t) \rangle + 2 \langle \delta n(t) \delta j_n(t) \rangle, \quad (12b)$$

863 where $\langle x_n \rangle$ and j_n denote $\langle x_n \rangle = \sum_{n=1}^{\infty} x_n \rho_n / \rho_c$ and $j_n = J_n / \rho_n$, respectively. In

864 equation (12b), the cross correlation, $\langle \delta n(t) \delta j_n(t) \rangle$, between n and j_n is defined by

$$865 \quad \langle \delta n(t) \delta j_n(t) \rangle = \langle n(t) j_n(t) \rangle - \langle n(t) \rangle \langle j_n(t) \rangle. \text{ Integrating equation (12b) with respect to time from}$$

866 t_0 to t and rearranging the resulting equation, we can obtain the following equation for the

$$867 \quad \text{relative variance, } \eta_n^2(t) (= \sigma_n^2(t) / \langle n(t) \rangle^2), \text{ when the mean-scaled correlation, } \langle \delta \tilde{n}(t) \delta \tilde{j}_n(t) \rangle$$

868 $[= \langle \delta n(t) \delta j_n(t) \rangle / \langle n(t) \rangle \langle j_n(t) \rangle]$ assumes its steady-state value:

$$869 \quad \eta_n^2(t) \cong \langle n(t) \rangle^{-1} + f(t_0) (\langle n(t_0) \rangle / \langle n(t) \rangle)^2 + \eta_n^2(\infty) \left[1 - (\langle n(t_0) \rangle / \langle n(t) \rangle)^2 \right], \quad (t > t_0) \quad (13)$$

870 where $f(t_0)$ denotes non-Poisson noise defined by $f(t_0) = \eta_n^2(t_0) - \langle n(t_0) \rangle^{-1}$. $\eta_n^2(\infty)$
871 denotes the steady-state value of $\eta_n^2(t)$, which is the same as the steady-state value of
872 $\langle \delta \tilde{n}(t) \delta \tilde{j}_n(t) \rangle$ (Supplementary Note 3 and Supplementary Fig. 24). In Supplementary Note 3,
873 we present the generalization of equations (12) and (13) for the case where $\rho_c(t)$ quickly
874 varies over time.

875 The accurate expression of J_n is complex when monomer association with
876 nanoparticles is a reversible diffusion-influenced reaction³², which is a non-Markov process
877 whose rate at a given time depends on the history of nanoparticle densities. However, when the
878 reversibility of monomer association with nanoparticles is small, J_n can be approximated by
879 the following simple formula:

$$880 \quad J_n(t) \cong k_n^a \rho_1(t) \rho_n(t) - k_{n+1}^d \rho_{n+1}(t) \quad (n \geq 1), \quad (14)$$

881 where k_n^a and k_{n+1}^d are the steady-state rate coefficients of the association reaction between
882 a monomer and an n -mer to form an $(n+1)$ -mer and the dissociation reaction of an $(n+1)$ -mer
883 into a monomer and an n -mer, respectively. Assuming that the reversibility of monomer
884 association with the nanoparticle is small, we use a generalization of the Collins-Kimball
885 formula³¹ to obtain k_n^a for monomer association with non-spherical nanoparticles, which is
886 given by

$$887 \quad k_n^a \cong \frac{A_n \kappa_a \cdot A_n D_1 / r}{A_n \kappa_a + A_n D_1 / r} = 4\pi \sigma_s^2 \kappa_a \frac{c_\delta n^{2/3}}{1 + \frac{\kappa_a \sigma_s}{D_1} n^{1/3}}, \quad (15)$$

888 where κ_a and D_1 respectively denote the bimolecular association rate parameter and the
889 monomer diffusion coefficient. In equation (15), A_n denotes the surface area of the n -mer,

890 which is related to the effective nanoparticle radius, $r [= \sigma_s n^{1/3}]$, by $A_n = 4\pi r^2 c_\delta$, where the
 891 shape factor, c_δ , is related to the shape index, δ , by (Supplementary Note 8)

$$892 \quad c_\delta = \frac{3(3^{1/2} - 1)(4 - \delta)\delta + 12 - 8 \cdot 3^{1/2}}{\pi^{1/3} (3\delta^3 - 18\delta^2 + 36\delta - 16)^{2/3}}. \quad (16)$$

893 k_n^a and k_{n+1}^d satisfy the detailed balance condition, $J_n = 0$ at equilibrium, or
 894 $k_n^a/k_{n+1}^d = q_{n+1}^*/q_n^*q_1^*$. Substituting the following expressions for the chemical potentials:
 895 $\exp(-\beta\mu_n^s) = q_{n+1}/q_n$ and $\exp[\beta\mu_1(t)] = \rho_1(t)/q_1^*$ into this detailed balance condition, we
 896 obtain $k_n^a = k_{n+1}^d \exp[-\beta(\mu_n^s - \mu_1(t))]/\rho_1(t)$. Using this equation, we can rewrite equation (14)
 897 as equation (2).

898 **Quantitative analysis of nanoparticle growth data.**

899 It is not easy to measure the absolute number densities, $\{\rho_n(t)\}$, of nanoparticles from our
 900 experimental data. However, we can measure the probability distributions,
 901 $\{p_n(t)[\equiv \rho_n(t)/\rho_c(t)]\}$, of nanoparticle size and the associated cumulative probability
 902 $\psi_n^p(t)[\equiv \sum_{k=n}^{\infty} p_k(t)]$, or the probability that a nanoparticle contains n or more monomers at
 903 time t . We can derive the hierarchical kinetic equations, (S4-1) for $\psi_n^p(t)$ from equations (11)
 904 (14) (Supplementary Note 4). In addition, we also derive a general relationship, equation (S3-
 905 14), between the mean and variance of the nanoparticle size (Supplementary Note 3). By
 906 comparing equations (S4-1) and (S3-14) with our experimental data for $\partial_t \psi_n^p(t)$ and $\sigma_n^2(t)$,
 907 we extracted the values of the adjustable parameters (Supplementary Note 4). The optimized
 908 values of the five time-independent adjustable parameters are presented in Supplementary
 909 Table 1 for each of the nanoparticle systems we investigated. The time profiles of the remaining

910 two time-dependent parameters, the degree, $\tilde{\rho}_1(t)$, of supersaturation and the shape index,
911 $\delta(t)$, are presented in Fig. 4b,c, respectively, for each system.

912 **Approximate analytic expression of nanoparticle size distribution.**

913 We found that, at all times, the experimental results for the nanoparticle size distribution,
914 $p_n(t)$, can be represented by the following formula:

915
$$p_n(t) \cong \frac{1}{(2\pi a_2^2)^{1/2}} e^{-(\ln n - a_1)^2 / 2a_2^2} \sum_{k=0}^{k_{\max}=6} b_k n^k, \quad (17)$$

916 which is a corrected version of a log-normal distribution⁵³. The values of parameters, a_1 , a_2 ,
917 and $\{b_0, b_1, \dots, b_6\}$, were calculated from our theory, i.e., by requiring the first six moments of
918 the nanoparticle size, calculated for our optimized model, to be the same as those of equation
919 (17). With the optimized values of the adjustable parameters at hand, we can easily calculate
920 the higher-order moments, $\langle n^q(t) \rangle$ ($q \geq 3$), using equation (S3-12), the analytical expression
921 of $\langle n^q(t) \rangle$ (Supplementary Note 3). This theoretical prediction is in good agreement with the
922 experimental results for these higher moments $\langle n^q(t) \rangle$ ($3 \leq q \leq 6$) at all times
923 (Supplementary Fig. 25). In addition, the results of equation (17) are in excellent agreement
924 with the experimentally measured size distributions, as shown in Fig. 2. The agreement
925 between theoretical prediction and experimental results for the higher order moments of
926 nanoparticle size and the nanoparticle size distribution demonstrates that our optimized model
927 is robust and can be used to predict various experimental results that are not used for model
928 optimization (see also Supplementary Fig. 26 for how sensitive the resulting model is to
929 variations in adjustable parameter values).

930 **Dynamics of coalescence between nanoparticles undergoing monomeric growth.**

931 To obtain the mathematical description of our coalescence model, we extended Lee and
 932 Karplus's reduced distribution function formalism for diffusion-influenced reactions between
 933 molecules to describe diffusion-influenced reactions between growing nanoparticles^{32,40}.
 934 According to this generalization, the nonequilibrium pair correlation between growing
 935 nanoparticles undergoing coalescence satisfies the following reaction-diffusion equation:

$$936 \quad \partial_t \rho(r, t) = D_r(t) \frac{1}{r} \partial_r^2 (r \rho(r, t)) - \kappa_{\bar{\sigma}(t)} S_{\bar{\sigma}(t)}(r) \rho(r, t), \quad (18)$$

937 where $\rho(r, t)$ denotes the nonequilibrium pair correlation function for a pair of nanoparticles
 938 separated by distance r at time t . In equation (18), the relative diffusion coefficient, $D_r(t)$,
 939 depends on time t because the mean nanoparticle size, inversely proportional to the diffusion
 940 coefficient, increases with time in our experiment. Here, the time profile of $D_r(t)$ was
 941 obtained from the experimental data by dividing the ensemble-averaged variance of the relative
 942 displacement, $\Delta \mathbf{r}_{ij}(t) [= \mathbf{r}_{ij}(t + t_0) - \mathbf{r}_{ij}(t_0)]$, in the two-dimensional TEM image by $4t$, where
 943 \mathbf{r}_{ij} is the relative position vector, $\mathbf{r}_{ij} = \mathbf{r}_i - \mathbf{r}_j$, with \mathbf{r}_i and \mathbf{r}_j indicating the positions of the
 944 i th and j th nanoparticles (Fig. 5g).

945 Ligand-passivated nanoparticles form an encounter pair, with a ligand-mediated
 946 nanoparticle contact, and then undergo fast coalescence. Here, the nanoparticle contact distance
 947 is given by the sum of the thickness, l , of the double ligand layer and the two metal core radii
 948 of the nanoparticles in the encounter pair. We denote the sum of the two metal core radii as σ .
 949 In equation (18), κ_σ and $S_\sigma(r)$ respectively denote the σ -dependent coalescence
 950 propensity and the reaction sink function accounting for the coalescence rate depending on the
 951 nanoparticle separation; they are explicitly given by

952
$$\kappa_\sigma = \frac{\kappa}{e^{\gamma(\sigma-\sigma_c)} + 1}, \quad (19a)$$

953
$$S_\sigma(r) = e^{-(r-\sigma-l)^2/2v}, \quad (19b)$$

954 with κ , γ , and v being constants. κ_σ , given in equation (19a), becomes vanishingly small when
 955 σ is much larger than the most probable core-core contact distance, σ_c , right before
 956 coalescence (Fig. 5d,h). In equation (19b), $S_\sigma(r)$ is the bell-shaped function centered on the
 957 contact separation, $\sigma + l$, between nanoparticles in the encounter pair. In equation (18), we
 958 have used the mean time-profile, $\bar{\sigma}(t)$, of the nanoparticle core-core contact distance,
 959 effectively accounting for the monomeric growth of the nanoparticle size (Supplementary Fig.
 960 27).

961 For a given set of the adjustable parameters, equation (18) can be numerically solved
 962 with the reflecting boundary condition, $\partial_r \rho(r,t) = 0$, at the moving boundary, $r = \bar{\sigma}(t)$, and
 963 the initial condition, $\rho(r,t=0) = \Theta(r-r_c)$ with $\Theta(x)$ denoting the unit step function
 964 defined by $\Theta(x \geq 0) = 1$ and $\Theta(x < 0) = 0$, which assumes that the initial distance between
 965 nanoparticles is larger than the cutoff distance, r_c (Supplementary Note 9 and Supplementary
 966 Fig. 28). With $\rho(r,t)$ at hand, we can obtain the coalescence rate coefficient,

967
$$k_f(t) = \int_{\sigma(t)}^{\infty} dr 4\pi r^2 \kappa_{\bar{\sigma}(t)} S_{\bar{\sigma}(t)}(r) \rho(r,t). \quad (20)$$

968 and the time dependent density of nanoparticles (Supplementary Note 10). By comparing the
 969 theoretical results with the experimental data for the time dependent density of nanoparticles,
 970 we determined the optimized values of the adjustable parameters (Supplementary Fig. 29 and
 971 Supplementary Table 2). The resulting profiles of the scaled coalescence propensity,

972 $\kappa_{\sigma}\rho_{c,T}(t_0)$, and the scaled coalescence rate coefficient, $k_f(t)\rho_{c,T}(t_0)$, with $\rho_{c,T}(t_0)$ denoting
973 the total nanoparticle density at initial time t_0 , are presented in Fig. 5h, c, respectively.

974 Finally, the distribution, $\psi(t)$, of the coalescence time presented in Fig. 5e can be
975 calculated from the time profile of $k_f(t)\rho_{c,T}(t_0)$ given in Fig. 5c (Supplementary Note 11).
976 In addition, from the time profile of $\psi(t)$, the distribution of the core-core contact distance
977 right before coalescence can be estimated. Our theoretical result for the distribution of the core-
978 core contact distance right before coalescence, presented in Fig. 5d, was calculated with the
979 time profile of $\psi(t)$ in Fig. 5e (Supplementary Note 11 for more details).

980

981 **Data availability**

982 All data used in the current research are available upon request to the corresponding authors.

983

984 **Code availability**

985 The MATLAB code and the Mathematica code used for our data analysis can be found at
986 <https://>

987

988 **Acknowledgements**

989 This work was supported by the Creative Research Initiative Project program
990 (2015R1A3A2066497) and the Engineering Research Center Program (NRF-
991 2020R1A5A1018052) funded by the National Research Foundation (NRF) of Korea; IBS-
992 R006-D1; the National Research Foundation (NRF) grant funded by the Korea government

993 (MSIT) (No. NRF-2017R1C1B2010434, No. NRF-2017R1A5A1015365, No. NRF-
994 2020R1A2C1102788, No. NRF-202117221036, and No. NRF-2021R1A2C1011797); the
995 MOTIE (Ministry of Trade, Industry & Energy) and KRSC (Korea Semiconductor Research
996 Consortium) support program for the development of future semiconductor devices (No.
997 10080657). S.J. and W.C.L. acknowledge the support from the research fund of Hanyang
998 University (HY-2018-N). B. Han acknowledges the Global Frontier Program through the
999 Global Frontier Hybrid Interface Materials (GFHIM) of the National Research Foundation of
1000 Korea (NRF) funded by the Ministry of Science and ICT (Project No. 2013M3A6B107888).

1001

1002 **Author contributions**

1003 J.-H.K., J.K., B.H.K., and S.S contributed equally to this work. B.H.K., J.K., S.J., W.C.L., T.H.,
1004 and J.P. planned the experimental portion of the research. J.-H.K., S.S., and J.S. planned the
1005 theoretical portion of the research. B.H.K., Y.S., and J.P. captured the TEM movies. J.K.
1006 conducted the image binarization. J.K., J.J., and K.P. conducted the particle tracking. B.H.K.,
1007 J.K., H.C., and J.W.J. conducted *ex-situ* experiments. B.H.K., J.K., S.J., H.C., B.H., W.C.L.,
1008 and J.P. conducted the analysis of experimental data. J.S., J.-H.K., and S.S. developed the
1009 model of a nanoparticle. J.S. developed the theory explaining nucleation, size-focusing, and
1010 defocusing of an ensemble of nanoparticles. J.S., J.-H.K., and S.S developed the theory
1011 explaining growth dynamics of an ensemble of nanoparticles. J.S. and J.-H.K. developed the
1012 analysis methods of the experimental data. S.S., Jingyu K., M.L. and J.-H.K. performed the
1013 quantitative analysis of the experimental data. J.S., J.-H. K., J.K., B.H.K., S.S., T.H.H, and J.P.
1014 wrote the manuscript. T.H.H. and J.P. supervised the experimental research. J.S. supervised
1015 the theoretical research. All authors contributed to the discussion of results.

1016

1017 **Competing financial interests**

1018 The authors declare no competing financial interests.

1019

1020 **Additional information**

1021 Supplementary information is available in the online version of this paper. Correspondence

1022 regarding the experiment should be addressed to T.H. and J.P. and correspondence regarding

1023 the theory and analysis to J.S.

1024

1025